Article

Neuron

Vasoactive Intestinal Polypeptide-Expressing Interneurons in the Hippocampus Support Goal-Oriented Spatial Learning

Highlights

- Ca^{2+} imaging indicates bimodal activity dynamics of VIP interneurons *in vivo*
- Activity of VIP interneurons is modulated by task and learning demands
- VIP-mediated disinhibition supports spatially guided reward learning

Authors

Gergely Farkas Turi, Wen-Ke Li, Spyridon Chavlis, ..., Boris Valery Zemelman, Panayiota Poirazi, Attila Losonczy

Correspondence

poirazi@imbb.forth.gr (P.P.), al2856@columbia.edu (A.L.)

In Brief

Turi et al. imaged activity of VIP-expressing interneurons of hippocampal area CA1 *in vivo*. They show learning-related reorganization in VIP population dynamics. VIP interneurons provide behavioral state-dependent disinhibition for CA1 pyramidal cells that supports spatial reward learning.

Turi et al., 2019, Neuron *101*, 1150–1165
March 20, 2019 © 2019 Elsevier Inc.
https://doi.org/10.1016/j.neuron.2019.01.009

CellPress

CellPress

Neuron
Article

Vasoactive Intestinal Polypeptide-Expressing Interneurons in the Hippocampus Support Goal-Oriented Spatial Learning

Gergely Farkas Turi,[1,9] Wen-Ke Li,[2,3,9] Spyridon Chavlis,[4,9] Ioanna Pandi,[4,5] Justin O'Hare,[2,3] James Benjamin Priestley,[2,3] Andres Daniel Grosmark,[2,3] Zhenrui Liao,[2] Max Ladow,[2] Jeff Fang Zhang,[2,3] Boris Valery Zemelman,[6,7] Panayiota Poirazi,[4,*] and Attila Losonczy[2,3,8,10,*]

[1]Department of Psychiatry, Columbia University, New York, NY 10032, USA
[2]Department of Neuroscience, Columbia University, New York, NY 10027, USA
[3]Mortimer B. Zuckerman Mind Brain Behavior Institute, Columbia University, New York, NY 10027, USA
[4]Institute of Molecular Biology and Biotechnology (IMBB), Foundation for Research and Technology-Hellas (FORTH), Heraklion, Crete 700 13, Greece
[5]School of Medicine, University of Crete, Heraklion, Crete 741 00, Greece
[6]Center for Learning and Memory, University of Texas, Austin, TX 78712, USA
[7]Department of Neuroscience, University of Texas, Austin, TX 78712, USA
[8]Kavli Institute for Brain Science, Columbia University, New York, NY, USA
[9]These authors contributed equally
[10]Lead Contact
*Correspondence: poirazi@imbb.forth.gr (P.P.), al2856@columbia.edu (A.L.)
https://doi.org/10.1016/j.neuron.2019.01.009

SUMMARY

Diverse computations in the neocortex are aided by specialized GABAergic interneurons (INs), which selectively target other INs. However, much less is known about how these canonical disinhibitory circuit motifs contribute to network operations supporting spatial navigation and learning in the hippocampus. Using chronic two-photon calcium imaging in mice performing random foraging or goal-oriented learning tasks, we found that vasoactive intestinal polypeptide-expressing (VIP$^+$), disinhibitory INs in hippocampal area CA1 form functional subpopulations defined by their modulation by behavioral states and task demands. Optogenetic manipulations of VIP$^+$ INs and computational modeling further showed that VIP$^+$ disinhibition is necessary for goal-directed learning and related reorganization of hippocampal pyramidal cell population dynamics. Our results demonstrate that disinhibitory circuits in the hippocampus play an active role in supporting spatial learning.

INTRODUCTION

The neocortex contains a diversity of GABAergic interneurons (INs) that play key roles in cortical computation. Classes of cortical GABAergic INs exhibit diverse morphological, molecular, and physiological characteristics and directly inhibit principal neurons at specific subcellular compartments such as the axon initial segment, soma, and different dendritic regions (Fishell and Rudy, 2011; Kepecs and Fishell, 2014). However, a distinct subset of INs also selectively targets other INs, resulting in disinhibition of principal cells (Letzkus et al., 2015; Pfeffer et al., 2013). This cortical disinhibition has been implicated in sensorimotor integration, attention, memory-guided behavior, gain control, and circuit plasticity (Fu et al., 2014; Kamigaki and Dan, 2017; Kuchibhotla et al., 2016; Lee et al., 2013; Letzkus et al., 2011; Pi et al., 2013; Zhang et al., 2014). A major subpopulation of disinhibitory INs express the vasoactive intestinal polypeptide (VIP) (Dávid et al., 2007; Kepecs and Fishell, 2014; Pfeffer et al., 2013) and has long been recognized as a potential disinhibitory circuit motif in the hippocampus (Acsády et al., 1996a, 1996b; Chamberland and Topolnik, 2012; Freund and Buzsáki, 1996; Gulyás et al., 1996; Pelkey et al., 2017; Tyan et al., 2014), a region critical for spatial and declarative learning (Eichenbaum, 2000; O'Keefe and Dostrovsky, 1971). While anatomical and *in vitro* physiological properties of hippocampal VIP$^+$ INs have been previously characterized (Tyan et al., 2014), we lack a basic description of their activity patterns in the behaving animal. Whereas structural plasticity of VIP$^+$ INs has been implicated in supporting spatial learning in the hippocampus (Donato et al., 2013), it is unknown how the functional dynamics of these disinhibitory cells contribute to learning. To address these questions, we performed *in vivo* two-photon Ca^{2+} imaging and optogenetic manipulations of VIP$^+$ INs in hippocampal area CA1, complemented by computational modeling of the CA1 circuit. We observed both behavior and learning-performance-related VIP$^+$ IN responses. Optogenetic manipulation of VIP$^+$ INs lead to alterations in learning performance and specific changes in CA1 spatial coding. Model simulations provided further insight into the possible origin of experimental results and point to a key disinhibitory role of VIP$^+$ IN in spatially guided reward learning.

RESULTS

Disinhibition of Pyramidal Cells by VIP$^+$ INs in Hippocampal Area CA1

To test whether VIP$^+$ INs exert a disinhibitory influence over CA1 pyramidal cells (CA1PCs), we first injected rAAV2/1:Syn-(ArchT-tdTomato)^{Cre} in area CA1 of the dorsal hippocampus in VIP-IRES-Cre mice. We confirmed that 96% of the Cre-expressing cells in this line were indeed immunopositive for VIP (Figure 1A). We next carried out whole-cell current-clamp recordings from CA1PCs in acute hippocampal slices and measured responses to electrical stimulation of Schaffer collateral inputs while optogenetically silencing CA1 VIP$^+$ INs on alternating trials (Figure 1B). We observed a significant increase in evoked post-synaptic inhibition on CA1PCs when VIP$^+$ INs were optogenetically silenced. To assess this disinhibition *in vivo*, we next injected rAAV2/9:EF1α-(bReaChES-tdTomato)^{Cre} along with rAAV2/1:CaMKII-GCaMP6f into CA1 in VIP-IRES-Cre mice to record Ca^{2+} activity in CA1PCs while optogenetically exciting VIP$^+$ INs with a red-shifted optogenetic actuator (Rajasethupathy et al., 2015). Mice were implanted with a head-post and imaging window above dorsal CA1 (Figure 1C, left; see STAR Methods; Dombeck et al., 2010; Lovett-Barron et al., 2014) and trained to run on a linear treadmill for a water reward during a random-foraging (RF) task (Danielson et al., 2016). We found that optogenetic activation of VIP$^+$ INs significantly increased the amplitude ($\Delta F/F$) and area under the curve (AUC, see STAR Methods) of identified Ca^{2+} transients in CA1PCs (Figures 1C and 1D), whereas CA1PCs in control mice injected with rAAV2/1:Syn-(tdTomato)^{Cre} and rAAV2/1:CaMKII-GCaMP6f showed no significant activity changes in response to light (Figures 1C, 1D, S2A, and S2B). Together, these results demonstrate that VIP$^+$ INs have a net disinhibitory role in regulating CA1PC activity.

Velocity and Spatial Modulation of VIP$^+$ IN Activity during Head-Fixed Spatial Navigation

We next sought to characterize the *in vivo* activity patterns of VIP$^+$ INs during behavior. We injected rAAV2/1:EF1α-(GCaMP6f)^{Cre} in dorsal CA1 of VIP-IRES-Cre mice and recorded Ca^{2+} dynamics of VIP$^+$ INs in behaving mice. We focused on VIP$^+$ INs in the CA1 *stratum pyramidale*, where the majority (53%) of these INs are located and identifiable as IN-targeting based on high level of calretinin (CR) (48%) and low level of cholecystokinin (CCK) co-expression (8%) (Figures S1A and S1B; Acsády et al., 1996a; Cea-del Rio et al., 2010; Somogyi et al., 2004; Tyan et al., 2014). We first assessed the modulation of VIP$^+$ INs by behavioral states. Head-fixed mice were trained to run on a cue-rich treadmill belt in a multisensory context for randomly administered water rewards (Figures 2A and 2B; random foraging [RF]; Danielson et al., 2016; Tyan et al., 2014). We found that Ca^{2+}activity was positively correlated with running velocity in 82% of VIP$^+$ INs with peak activity lagging the animal's velocity (Figure 2B). In the remaining 18% of cells, Ca^{2+} activity showed shorter latency and negative correlation with velocity (Figures 2B and S2C). Therefore, we partitioned the VIP$^+$ IN population into two functional groups for subsequent analysis: positively velocity modulated (PVM) and negatively velocity modulated (NVM), based on the sign of peak correlations with velocity (Figures 2A and 2B; PVM: red, NVM: blue). We found that this classification was relatively stable from day to day during RF (Figure S2D).

The short-latency, negative velocity correlations in the NVM group implied that these cells were more active after the animal stopped running. To investigate this further, we examined changes in the activity of VIP$^+$ INs aligned to the onset and offset of locomotion (Figures 2C–2E and S2E). We calculated the response reliability of each cell to these events (see STAR Methods) and found that most VIP$^+$ INs in the PVM group (Figure 2C, top) showed either an increase or no change in Ca^{2+} activity after running start, and decreased Ca^{2+} activity after running stop. The NVM group showed the converse relationship (Figure 2C, bottom). To determine whether VIP$^+$ IN responses to locomotion are transient or persistent during steady-state locomotion, we compared the mean $\Delta F/F$ for each neuron during periods of prolonged ($\geq$9 s) running or resting (see STAR Methods). The majority (76%) of PVM VIP$^+$ INs displayed reliably elevated activity when the animal was running, while 42% of NVM VIP$^+$ INs reliably decreased their Ca^{2+} activity; the remaining (58%) showed no reliable change (Figure 2F). In addition, we observed significant spatial tuning in a subset of CA1 VIP$^+$ INs during RF (29%; Figure S2G). Together, these results demonstrate that, similar to other hippocampal IN subtypes (Arriaga and Han, 2017; Fuhrmann et al., 2015; Grienberger et al., 2017; Lapray et al., 2012; Lovett-Barron et al., 2014; Somogyi et al., 2013), a majority of VIP$^+$ INs are strongly and positively modulated by locomotion while a subset showed negative modulation. By comparison, parvalbumin-expressing (PV$^+$) INs in the CA1 *stratum pyramidale* of PV-IRES-Cre mice exhibited a more homogeneous, positively modulated velocity response profile (99.4% of cells) while a small proportion of somatostatin-expressing (SOM$^+$) INs (8.4%) in the CA1 *stratum oriens* in SOM-IRES-Cre mice also displayed strong negative modulation by locomotion (Figure S3A; Arriaga and Han, 2017). Interestingly, the negatively correlated SOM$^+$ INs exhibited more negative modulation than VIP$^+$ INs in the NVM group (2-sample t test on Fisher Z-Transformation of r values, $t = 4.56$, $p = 0.00014$, data not shown). Also congruent with PVM response profiles, simultaneous imaging and local field potential recordings revealed that PVM activity was more correlated than NVM activity with running-associated theta band (5–10 Hz) power (Figure S3B).

These functionally identified groups of VIP$^+$ INs could possibly align with neurochemically defined subgroups of VIP$^+$ INs expressing CR or CCK; the latter specifies a subset of INs that target the perisomatic region of pyramidal cells (VIP$^+$/CCK$^+$ basket cells) (Acsády et al., 1996a; Somogyi et al., 2013; Tyan et al., 2014) and represents a small fraction of the VIP$^+$ INs in the CA1 pyramidal layer (8%; Figure S1B; Tyan et al., 2014). Therefore, we computed the fraction of all imaged VIP$^+$ INs that belonged to each functional group and compared these to the fractions from neurons identified by post hoc immunostaining of secondary neurochemical markers (Figure S1C). We found that CCK-negative VIP$^+$ INs (CR-positive or CR-negative) showed PVM-NVM fractions similar to the total recorded population, suggesting that the majority of PVM VIP$^+$ INs are disinhibitory VIP$^+$ INs. In contrast, within the CCK-positive VIP$^+$ INs, the NVM group was significantly enriched (Figure S1D). Together, these results show heterogeneous locomotion-related

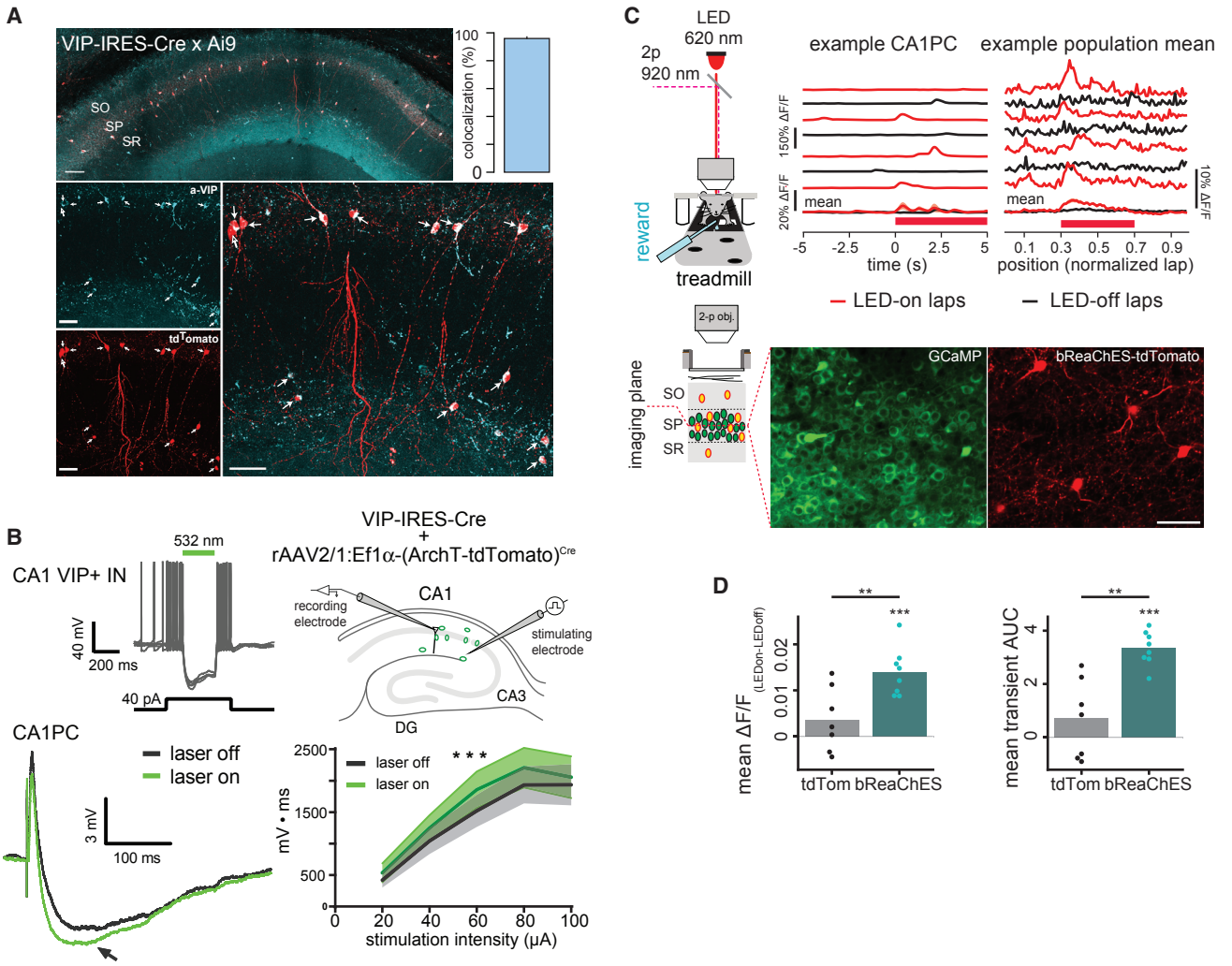

Figure 1. VIP$^+$ INs Disinhibit Pyramidal Cells in Hippocampal Area CA1

(A) Immunocytochemical characterization of VIP-IRES-Cre mice. VIP (blue) was detected in 96% ± 1.3% (mean ± SD) of tdTomato-expressing (red) neurons in CA1 in VIP-IRES-Cre mice crossed with Ai9 reporter mice (4 mice, 613/641 cells, inset). Filled arrows: double-labeled cells; empty arrow (top left corner): VIP-negative cell in *stratum pyramidale* (SP). Scale bar: 50 μm. SO, *stratum oriens*; SR, *stratum radiatum*.

(B) Optogenetic silencing of VIP$^+$ INs increases inhibitory post-synaptic potentials (IPSPs) in CA1PCs *in vitro*. Top left: overlaid current-clamp traces show responses (5 trials) of an ArchT-expressing VIP$^+$ IN to depolarizing somatic current injection (40 pA, bottom trace) with an interposed 532 nm laser pulse (green bar). Top right: experimental setup to assess impact of VIP$^+$ IN activity on CA1PCs. In acute hippocampal slices expressing ArchT in VIP$^+$ INs, CA1PC responses to single-pulse electrical stimulation of CA3 Schaffer collaterals in CA1 SR were recorded in current-clamp with 532 nm light delivered on alternating trials. Bottom left: example traces showing CA1PC response to consecutive trials with laser off (gray) and on (green). Arrow: IPSP following short-duration excitatory postsynaptic potential. Bottom right: Integrated inhibitory responses are larger during photo-inhibition of VIP$^+$ INs (2-way, repeated-measures [RM] ANOVA: $F(1,15) = 23.98$, $p = 0.00019$, $n = 16$ cells, interaction: $p = 0.17$). Data are presented as mean ± SEM.

(C) Optogenetic activation of VIP$^+$ INs increases CA1PC activity *in vivo*. Left: *in vivo* 2-photon imaging and simultaneous optogenetic stimulation setup. The mouse is head-fixed under a 2-photon microscope and is allowed to run freely on a treadmill. Red-shifted channelrhodopsin variant bReaChES was expressed in CA1 VIP$^+$ INs via rAAV2/1:EF1α-(bReaChES-tdTomato)^{Cre} and activated with an LED (620 nm). CA1PCs were labeled with pan-neuronal GCaMP6f via rAAV2/1:CaMKII-GCaMP6f (Nathanson et al., 2009; Scheyltjens et al., 2015; Schoenenberger et al., 2016). Middle: single-plane, 2-photon, time-averaged image showing widespread expression of GCaMP6f (green) and bReaChES (red) in neuronal elements including VIP$^+$ INs in CA1 SP (scale bar: 50 μm). CA1PC Ca^{2+} activity was recorded during alternating laps with LED turned on (LED-on) and off (LED-off) then compared for each cell. Middle top: example Ca^{2+} ΔF/F traces from a CA1PC. Black: LED-off laps, red: LED-on laps. Red bar at bottom: LED activation area for LED-on laps; middle bottom: mean ± SEM of ΔF/F traces. Right: example population mean for ΔF/F traces of all CA1PCs in a single field of view (FOV) for individual LED-on and LED-off laps (average of n = 107 CA1PCs per FOV). Bottom right: mean ± SEM of ΔF/F during LED-on laps and LED-off laps for the FOV for that session.

(D) Quantification of changes in CA1PC Ca^{2+} activity between LED-on and LED-off laps. Left: mice expressing bReaChES in VIP$^+$ INs displayed a greater change in mean ΔF/F in response to photostimulation compared to tdTomato controls ($t = 3.03$, $p = 0.009$, $\alpha = 0.016$). Right: mice expressing bReaChES in VIP$^+$ INs also showed a greater increase in transient AUC relative to controls ($t = 4.18$, $p = 0.003$, $\alpha = 0.016$).

See also Figures S1–S4.

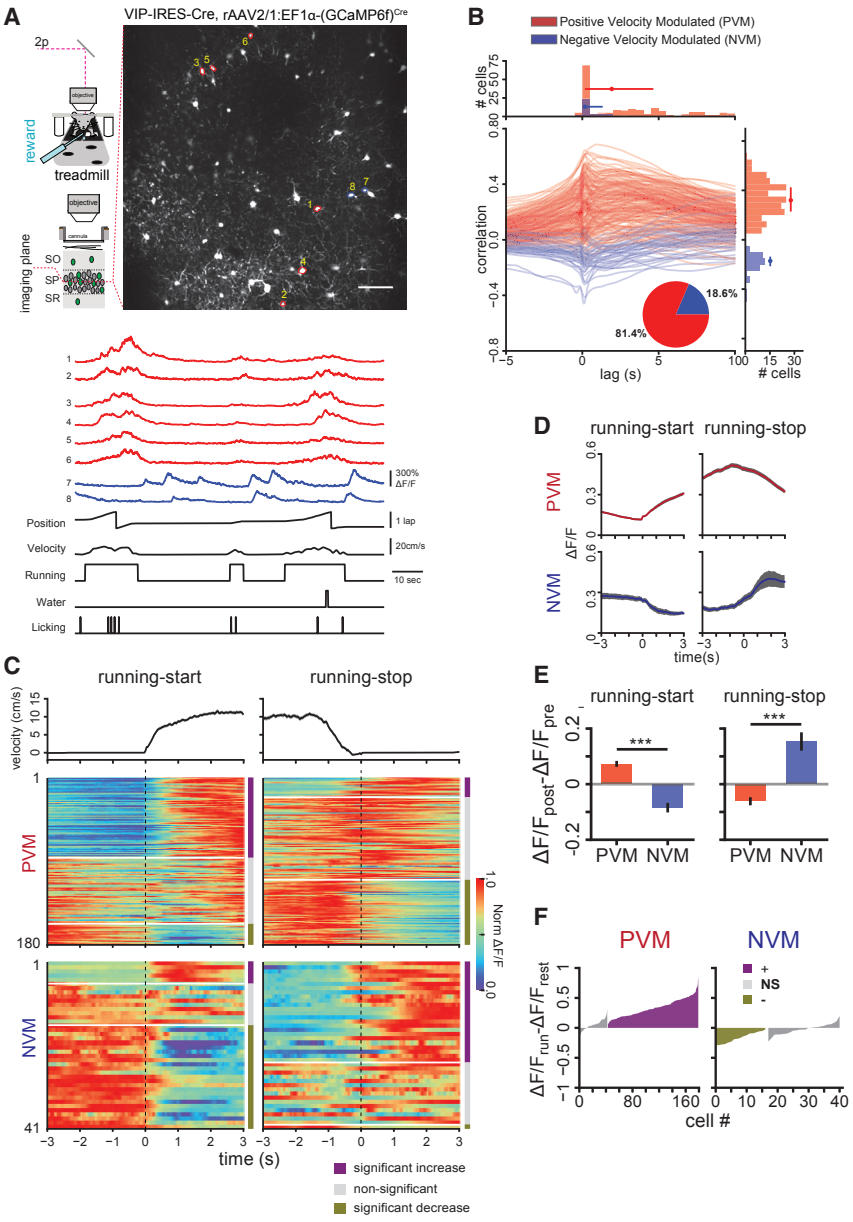

Figure 2. VIP$^+$ INs Exhibit Two Distinct Response Profiles during Locomotion

(A) Top: example FOV showing GCaMP6f-expressing VIP$^+$ INs in CA1 SP (scale bar: 100 μm). Bottom: example ΔF/F traces from the marked VIP$^+$ INs in FOV above with associated behavior variables (black traces). Ca^{2+} traces are color coded by the classification in (B).

(B) Cross-correlation between VIP$^+$ IN ΔF/F signals and animal's velocity. Each line is the velocity cross correlation of one cell (221 cells, n = 5 mice, 44 ± 16 cells/mouse, mean ± SD). Right: distribution of peak correlation values. Cells were separated into two groups based on this distribution: positive velocity modulated (*PVM*, red, 180/221 cells, 36 ± 12 cells/mouse, mean ± SD) and negative velocity modulated (*NVM*, blue, 41 cells, 8 ± 5 cells/mouse, mean ± SD). Circle and vertical bar: median and interquartile range, respectively (*PVM:* 0.32 [0.23 to 0.42], *NVM:* −0.17, (−0.21 to −0.14). Inset: relative proportions of cells in both groups. Top: distribution of time lag at peak correlation (*PVM:* 1.92 s (0.17 to 4.65), *NVM:* 0.17 s (0.13 to 1.33), median (inter-quartile range).

(C) VIP$^+$ IN responses to running-start (left, n = 261 events, 5 mice, 52 ± 12 events per mouse, mean ± SD) and running-stop events (right, n = 170 events, 5 mice, 34 ± 17 events per mouse, mean ± SD). Top: velocity mean ± SEM of locomotion events. Middle: responses of PVM VIP$^+$ INs (same 180 cells for both event types). Each row is the peak-normalized mean ΔF/F of a cell. Cells are sorted by the statistical significance of their responses to the events (see STAR Methods). Bottom: responses of NVM VIP$^+$ INs (same 41 cells for both event types). Time is relative to the onset of the locomotion event.

(D) Mean ± SEM peri-stimulus time histogram of PVM (top) and NVM (bottom) VIP$^+$ INs triggered by running start (left) and running stop (right).

(E) Amplitude of PVM and NVM VIP$^+$ IN responses (mean ± SEM) to running-start (left: t = 7.77, p = 3.42×10^{-11}) and running-stop events (right: t = 5.95, p = 1.74×10^{-7}) are significantly different between the two groups ($\alpha = 0.025$).

(F) Modulation magnitude of Ca^{2+} activity in VIP$^+$ IN subgroups during steady state locomotion (see STAR Methods).

See also Figures S2–S4.

response profiles in CA1 VIP$^+$ INs, where the majority of cells are positively modulated by velocity and a subset show negative velocity modulation.

VIP$^+$ IN Activity Is Modulated by Reward and Spatial Location during Goal-Oriented Learning

We next explored whether VIP$^+$ IN activity is modulated by features of spatial navigation beyond locomotion. To this end, we trained mice in a head-fixed goal-oriented learning (GOL) task (Figure 3A; see STAR Methods) in which operant water rewards are delivered at a fixed treadmill location and mice learn to lick selectively near this "hidden" reward location (Figure 3A; Danielson et al., 2016; Zaremba et al., 2017). We recorded the activity of the same VIP$^+$ INs (n = 253 cells) throughout the GOL task and classified these cells into PVM and NVM groups (Figure 3B) as in RF. VIP$^+$ INs showed similar overall stability from day to day compared to RF (Figure S2D, GOL). However, since mice must learn and remember the location of the goal zone and lick actively to receive reward, we expected that VIP$^+$ INs might respond differently to expected reward delivery compared to RF. Indeed, the fraction of cells that reliably changed their activity (Figures 3C and 3D) in response to reward delivery was significantly higher for the GOL task (90%) compared to RF (44%) (Figures 3C and 3D), but the level of responses is not significantly different between tasks (Figure S2F).

Once the task is learned, mice run toward the reward location and then briefly stop in the reward zone during the time of the reward delivery, which can result in mixed locomotion and

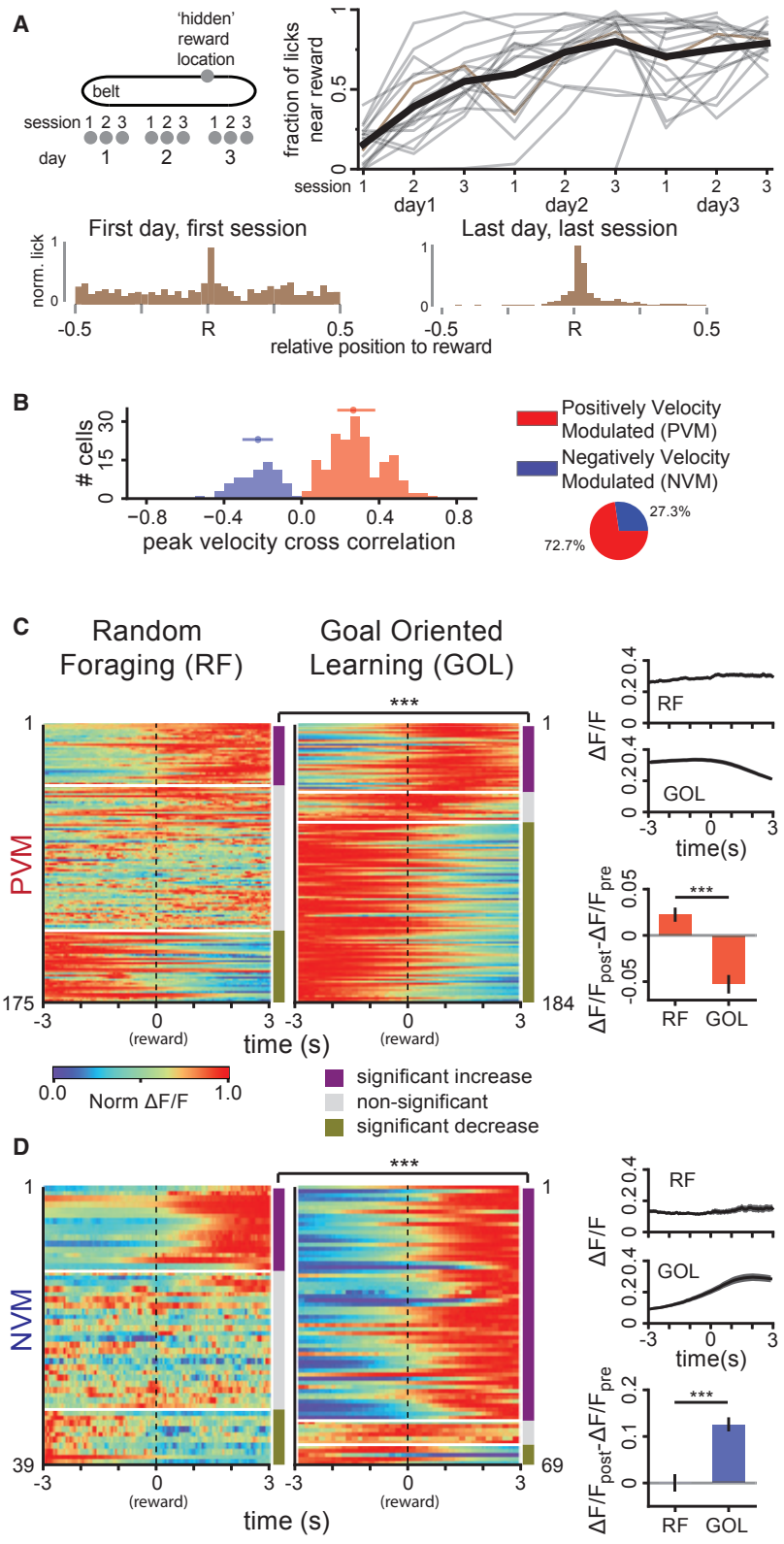

Figure 3. VIP⁺ INs Are Modulated by Reward during Spatially Guided Reward Learning

(A) Goal-oriented learning (GOL) task. Left: a water reward is operantly delivered at a fixed 10 cm long, non-cued location on the belt. Mice ran for 3 × 10 minute sessions per day for 3 days. Right: mice learned to selectively lick near the location of the reward (bottom inserts, distribution of licks on the belt) (n = 10 mice, 17 ± 1 sessions/mouse for 9 mice, 9 sessions for one mouse).

(B) Distribution of peak cross-correlation between velocity and VIP⁺ IN Ca^{2+} activity in the GOL task (n = 253 cells, 10 mice, 25 ± 15 cells/mouse, mean ± SD), grouped as PVM (red, 184 cells, 18 ± 12 cells/mouse, mean ± SD, median correlation: 0.27 [0.18 to 0.67], median [interquartile range]) and NVM (blue, 69 cells, 7 ± 4 cells/mouse, mean ± SD, correlation: −0.22 [−0.31 to −0.15]) groups as in RF.

(C) PVM VIP⁺ IN responses to reward delivery events. Left: random foraging (RF; 175 cells); middle: GOL (184 cells). Each row is the peak-normalized mean ΔF/F of a cell triggered by reward delivery events normalized by the cell's maximum, sorted by statistical significance of responses (see STAR Methods). The proportions of cells in each response group are significantly different between RF and GOL (χ^2 test, χ^2 [2, N = 359] = 105.6, $p = 1.2 \times 10^{-23}$). Right top: peri-stimulus time histogram (PSTH) of PVM VIP⁺ INs in RF and GOL tasks triggered by reward delivery. Bottom: mean ± SEM amplitude of PVM VIP⁺ IN transients in RF and GOL tasks (t = 5.34, $p = 6.3 \times 10^{-9}$).

(D) NVM VIP⁺ IN responses as in (C) (RF: 39 cells, GOL: 69 cells). The proportion of cells in each response group are significantly different between RF and GOL (χ^2 test, χ^2 [2, N = 108] = 37.1, $p = 8.8 \times 10^{-9}$). Right bottom: mean ± SEM of NVM VIP⁺ IN transient amplitudes in RF and GOL tasks (t test, t = −5.3, $p = 7.1 \times 10^{-7}$).

For χ^2 tests and t tests in (C) and (D), $\alpha = 0.025$. See also Figures S2–S4.

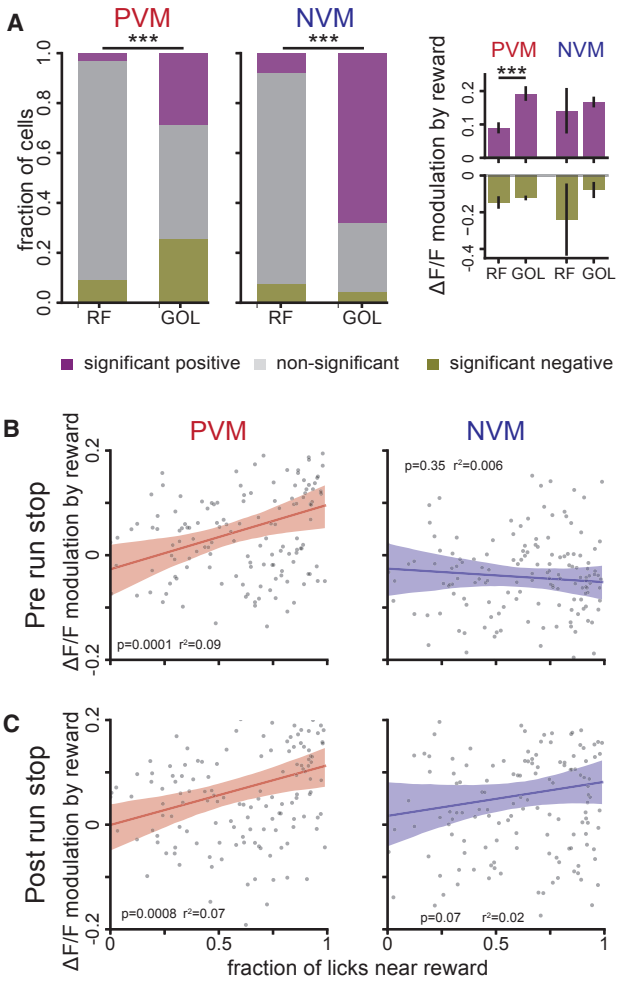

Figure 4. Task-Dependent Modulation of Running-Stop Responses of VIP⁺ INs by Reward

(A) Left: fractions of cells whose running-stop responses are significantly modulated by reward delivery (see STAR Methods). PVM: χ^2 test, χ^2 (2, N = 359) = 71.1, p = 3.6 × 10^{-16}, NVM: χ^2 (2, N = 114) = 33.7, p = 4.8 × 10^{-8}, α = 0.025. Right: transient amplitude modulation (mean ± SEM) for significant positive cells (top, purple, PVM: t = −3.8, p = 0.0009, NVM: t = −0.45, p = 0.69) and significant negative cells (bottom, olive, PVM: t = −0.98, p = 0.33, NVM: T = −0.8, p = 0.5), α = 0.0125.

(B and C) Reward modulation of transient amplitude before (B) and after (C) running-stop events in the GOL task show significant correlation (α = 0.0125) with behavior for PVM but not NVM VIP⁺ INs. Each point is the mean modulation of the cells in a session and the licking performance of that session. Shaded region: 99% bootstrap confidence interval of the least-squares linear fit.

See also Figure S4.

reward-related Ca^{2+} responses in VIP⁺ INs. To isolate the locomotion-related and reward-related components, we first analyzed how reward delivery modulated responses during running-stop events only. We found that a significantly larger fraction of cells was modulated by reward delivery in the GOL task compared to RF (Figure 4A, left). Significantly modulated VIP⁺ INs in the NVM group were predominantly positively modulated by reward, while PVM VIP⁺ INs did not show bias to either direction however the reward-related transients in the positively modulated groups were significantly higher in the GOL task (Figure 4A, right). Together, these results indicate that the spatial memory-dependent GOL task accentuates the responses of VIP⁺ INs during running stops in the presence of reward.

To investigate whether reward responses in GOL are modulated by learning, we correlated the modulation of the Ca^{2+} activity in VIP⁺ INs during rewarded and unrewarded running-stop events with learning performance. Reward modulation of the mean Ca^{2+} activity for 3 s before (Figure 4B) and 3 s after (Figure 4C) running-stop events was positively correlated with learning performance in PVM but not NVM VIP⁺ INs. However, velocity preceding 3 s of running-stop events was also significantly higher for rewarded compared to unrewarded events (Figure S3C), which raised the question of whether the observed correlations in the PVM group are due to reward modulation of velocity or to reward delivery. To control the effect of reward modulation over velocity, we computed the partial correlation between reward modulation of VIP⁺ IN running-stop activity and learning performance (see STAR Methods; Figure S3D) and found that the positive correlation in Figure 4 remained. These results indicate that the running-stop responses of VIP⁺ INs in GOL are modulated by reward beyond the modulation explained by locomotion.

We additionally designed a model-based approach to isolate the specific contributions of behavioral covariates for predicting the activity of VIP⁺ INs and predict whether these relationships changed with learning in the GOL task. We used a generalized linear model (GLM) (Allen et al., 2017; Pinto and Dan, 2015) to fit VIP⁺ INs Ca^{2+} activity as a linear function of all behavioral variables (Figure 5A; see STAR Methods). Behavioral variables predicted a similar fraction of variance in both PVM and NVM VIP⁺ IN groups (Figure 5B, left, r^2: PVM: 0.28 (0.18–0.40), NVM: 0.27 (0.17–0.39) median (interquartile range); 2-sample t test, t = 0.74, p = 0.45, α = 0.05). We next divided the behavioral variables into 3 groups (reward, locomotion, and position) and computed the predictive information each variable group contributed to the model via a cross-validated log likelihood ratio (LLR) approach (Figure 5B, right; see STAR Methods). Each group contributed some independent information about VIP⁺ IN activity, congruent with our prior result that reward modulation is not fully explained by locomotion. Similarly, we found that the independent information gained from locomotion and reward variables exhibited negative and positive correlations respectively with learning performance of the animals (Figure 5C). This analysis demonstrates that reward-related variables become increasingly predictive of VIP activity as animals learn, beyond the expected change from differences in the other behavioral parameters.

Since the position variables were most informative (Figure 5B), we further examined their contribution during learning. Information gained from position was only weakly correlated with learning performance (Figure 5D). However, we found that positions around the reward zone contributed the largest source of information (Figure 5D). While the information gained from positions at the reward zone was not significantly correlated with learning performance, the information from positions away from the reward zone was negatively correlated (Figure 5E).

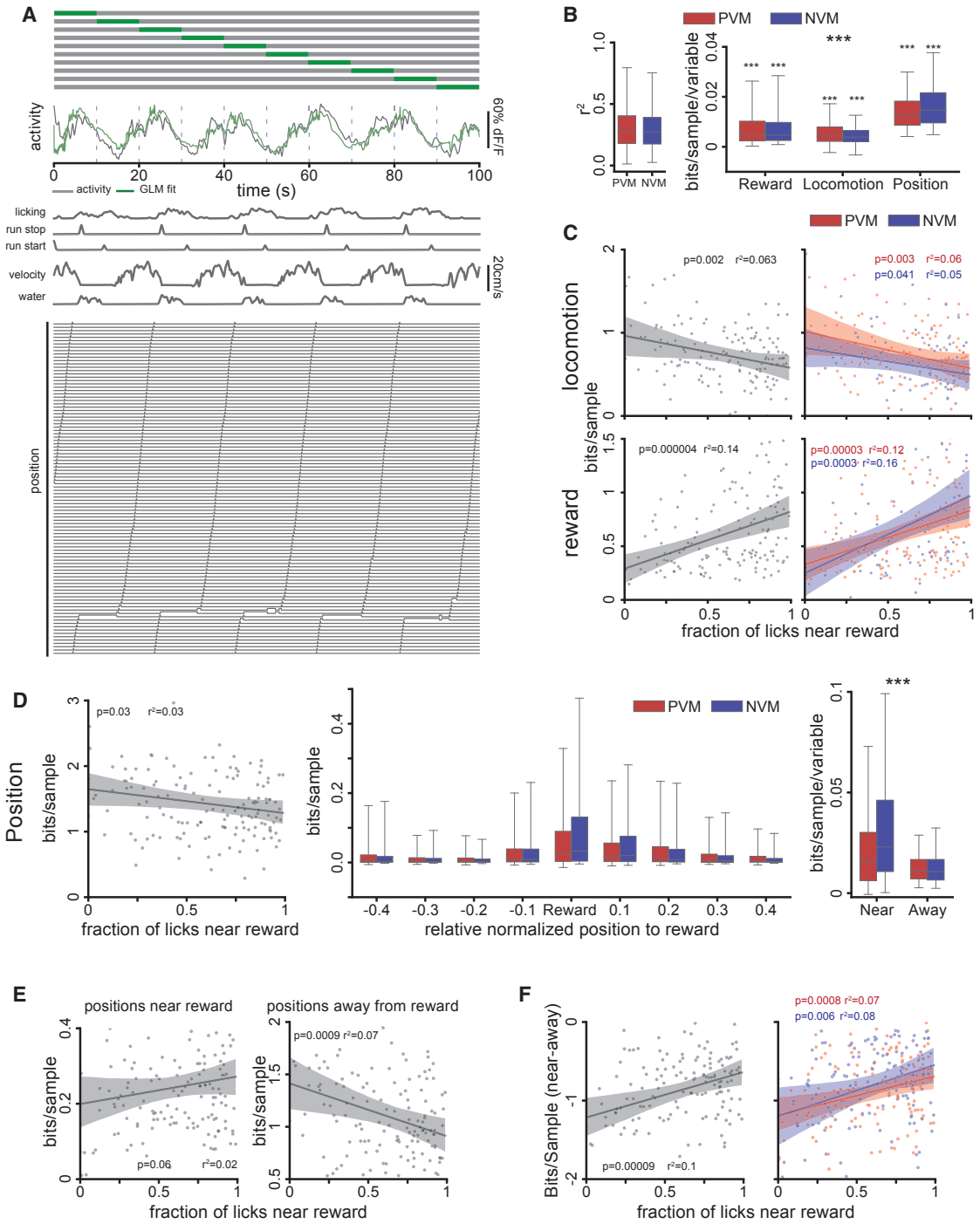

Figure 5. Influence of Locomotion, Reward, and Position on VIP⁺ IN Activity during Learning

(A) Schematic of the generalized linear model (GLM) with example behavioral predictors and model fit. Top: example 10-fold cross-validation (CV) of the model on 100 s of activity. Each row is a fold; gray and green indicate data used for training and testing, respectively. Middle: example activity of a cell and GLM predictions. Bottom: behavior variables used for fitting the activity (see STAR Methods).

(B) Left: distribution of r^2 between the activity and the GLM prediction calculated for each cell, reported for PVM and NVM cell groups (2,942 cell sessions, 250 cells, 11 ± 5 sessions per cell, mean ± SD). Right: information gained (LLR, see STAR Methods) for predicting VIP⁺ IN activity by including each category of behavior signals in the model (reward: PVM: 0.005 [0.002–0.01], NVM: 0.005 [0.003–0.01], Locomotion: PVM: 0.004 [0.002–0.008], NVM: 0.004 [0.002–0.007], Position: PVM: 0.013 [0.008–0.018], NVM: 0.015 [0.01–0.022], median [interquartile range]). The predictive information contributed independently by each variable category is significantly different from zero (1-sample t test, $\alpha = 0.0083$. Reward: PVM: $t(2072) = 37.83$, $p = 1.32 \times 10^{-238}$, NVM: $t(596) = 20.27$, $p = 7.19 \times 10^{-70}$. Locomotion: PVM: $t(2072) = 37.05$, $p = 4.89 \times 10^{-231}$, NVM: $t(596) = 19.19$, $p = 2.93 \times 10^{-64}$. Position: NVM: $t(2072) = 69.24$, $p < 1.0 \times 10^{-300}$, PVM: $t(596) = 36.75$, $p = 2.66 \times 10^{-155}$).

(legend continued on next page)

Correspondingly, the difference in information gained between near and away positions was significantly positively correlated with learning performance (Figure 5F). These results indicate that, as the performance of the animal increased during the GOL task, VIP$^+$ INs are increasingly more responsive to the reward and reward position-related variables.

Monosynaptic Inputs to CA1 VIP$^+$ INs

To explore potential anatomical sources of reward-related and space-related signals to CA1 VIP$^+$ INs, we used monosynaptic retrograde rabies virus tracing (Reardon et al., 2016; Figure S4). We found high numbers of presynaptic cells in reward-related neuromodulatory subcortical nuclei, including the septal and medial raphe nuclei, and scattered labeling in the ventral tegmental area. Hippocampal areas such as CA1, CA2, and CA3 and entorhinal-perirhinal regions (Figure S4K) contained high to moderate number of presynaptically labeled cells. Thus, CA1 VIP$^+$ INs receive diverse inputs from hippocampal, cortical, and subcortical sources capable of transmitting reward- and position-related information.

Optogenetic Manipulation of VIP INs Alters Learning Performance and Place Cell Enrichment

If positive modulation of VIP$^+$ IN activity by reward delivery plays an active role in spatially guided reward learning, then manipulating the activity of these local disinhibitory INs may alter learning performance in the GOL task. We tested this hypothesis via optogenetic manipulation of VIP$^+$ INs. VIP-IRES-Cre mice were injected bilaterally in CA1 with a Cre-dependent rAAV, driving expression of either channelrhodopsin (VIP-ChR2, 4 mice), archaerhodopsinT (VIP-ArchT, 9 mice), or GFP (VIP-GFP, 7 mice) and then implanted with optic fibers above dorsal CA1 (Figure S5A). Mice were trained in the GOL task for 3 consecutive days for one reward location without optogenetic manipulation and showed similar learning performance across groups (Figure 6A, days 1–3). Subsequently, mice were trained on a new reward location for the next 3 days, where we applied laser stimulation in a 70 cm segment of the belt centered around the new reward zone to increase (ChR2) or decrease (ArchT) activity of VIP$^+$ INs (Figure 6A, days 4–6; see STAR Methods). Licking and locomotion were similar between groups (Figure S5B), indicating that our manipulations did not impair the animals' ability to run or to seek reward. We found that VIP-ChR2 mice learned significantly faster than VIP-GFP controls, whereas VIP-ArchT mice achieved significantly worse performance (Figure 6A).

We next investigated how peri-reward VIP$^+$ IN activity might regulate CA1PC dynamics during learning. Previous studies have demonstrated (Danielson et al., 2016; Dupret et al., 2010; Gauthier and Tank, 2018; Zaremba et al., 2017) that CA1PC place cells over-represent reward locations during the GOL task and that the magnitude of place cell enrichment predicts learning performance. We hypothesized that, if peri-reward VIP$^+$ IN activity near reward is involved in this recruitment, then inhibiting VIP$^+$ INs should impair the recruitment of extra place cells near the reward (Figure 6B). Figures 6E and 6F show that, given the laser stimulation in the 70 cm of the belt centered around the reward during learning, the VIP-GFP mice (n = 7) showed enrichment of place cells near the reward after learning, while the enrichment was absent in VIP-ArchT mice (n = 5). We did not observe a significant difference between the transient rate or transient AUC of CA1PC place cells (Figure 6C), the fraction of place cells, or the width of place fields between VIP-GFP and VIP-ArchT mice (Figure 6D). Notably, optogenetically enhanced VIP$^+$ disinhibition was insufficient to induce reorganization of CA1PCs place cells in a fixed, unrewarded zone of the treadmill belt during the RF task (Figure S5C). Together, these results indicate that VIP$^+$ IN-mediated disinhibition is necessary, but not sufficient, to drive learning performance-related reorganization of CA1PC activity during learning.

Computational Modeling of the Disinhibitory Effect of CA1 VIP INs

As VIP$^+$ INs can have both direct (inhibitory) and indirect (disinhibitory) effects on CA1PC activity depending on CCK expression, we sought to clarify the interpretation of our experimental observations by developing a detailed biophysical model of the CA1 circuit that could dissect the contributions of different subgroups of VIP$^+$ INs to spatial encoding. Our model, consisting of CA1PCs and six types of INs, was validated against experimental data with respect to passive and active electrophysiological properties, connectivity profiles, and input patterns (Figures 7A, 7B, and S6; STAR Methods). To generate place-cell-like activity in model CA1PCs as in GOL, we introduced convergent entorhinal cortical (EC) input as multiple grids covering a virtual linear track (Figure 7C; see STAR Methods). The effect of reward-based learning was simulated as an increase in the strength of EC and CA3 connections onto all CA1PCs whose

Predictive information also differed between variable categories according to group (bits/(sample×number of variables), 2-way RM ANOVA, categories: $F(2, 476) = 395.3$, $p = 6.8 \times 10^{-102}$, n = 240 cells, groups: $F(1, 238) = 0.053$, $p = 0.82$, interaction: $F(2, 476) = 51$, $p = 8.47 \times 10^{-22}$, $\alpha = 0.05$).

(C and D) Information gained from the three categories of behavioral signals is correlated with learning ($\alpha = 0.0055$, nine tests: three for each category). Each point represents the average information gain for cells in a session and the corresponding licking performance of the animal in that session (see Figure 3A).

(C) Top: locomotion-related variables. Left: all VIP$^+$ INs; right: NVM and PVM groups. Bottom: reward-related variables.

(D) Left: information gained from all position variables is not correlated with learning (PVM and NVM groups not shown). Information gain is highest in the reward zone (middle). Right: the information gain from positions near the reward (10% of the lap centered around the reward zone) is significantly different from that gained from positions away from the reward (2-way RM ANOVA, positions: $F(1, 248) = 116.4$, $p = 1.7 \times 10^{-22}$, groups: $F(1, 248) = 11.5$, $p = 0.0008$, interaction: $F(1, 248) = 0.25$, $p = 0.61$, $\alpha = 0.05$).

(E) Positions near the reward have a weak positive correlation with performance (left), while positions away from the reward have a stronger and significant ($\alpha = 0.025$) negative correlation with performance (right).

(F) The difference between information gain from positions near and away from the reward zone (near-away) is positively correlated with learning. Left: all VIP$^+$ INs, right: VIP$^+$ INs divided by PVM and NVM groups ($\alpha = 0.016$).

See also Figure S4.

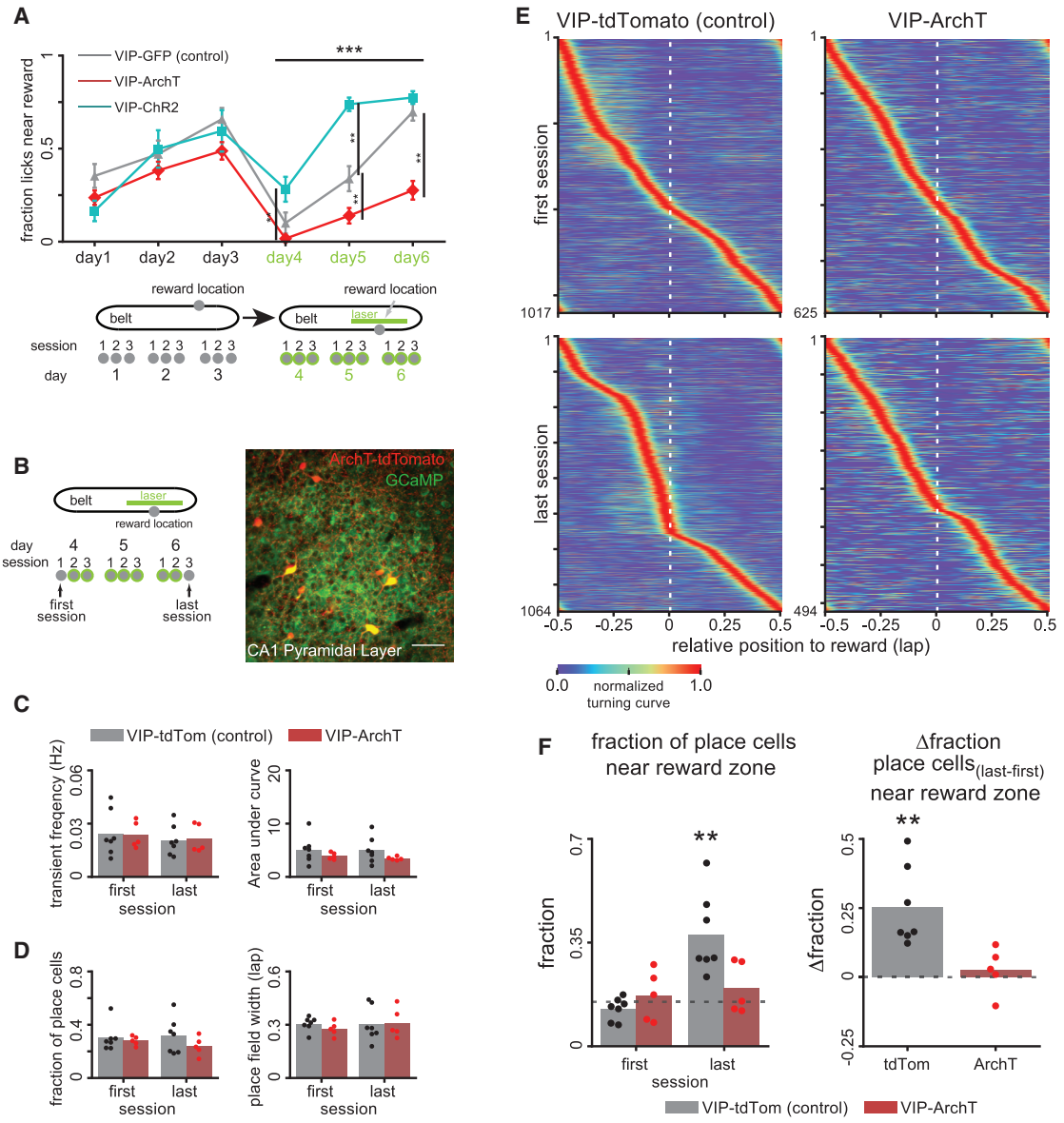

Figure 6. Inhibiting VIP$^+$ INs Impairs Goal-Directed Enrichment of Place Cells during the GOL Task

(A) Optogenetic manipulation VIP$^+$ IN activity bidirectionally affects learning performance in the GOL task. Top: performance measured by fraction of licks near reward location. Bottom: schematic of training schedule. VIP-GFP, (7 mice), VIP-ArchT (9 mice), and VIP-ChR2 (4 mice) performance on the first reward zone was not significantly different (2-way RM ANOVA). Group performance on the second reward zone was significantly different (2-way RM ANOVA: groups: $F(2, 15)$: 12,23, $p = 0.0007$, $n = 20$ mice, days: $F(2, 34)$: 74.6, $p = 3.7 \times 10^{-13}$, interaction: $F(4, 34) = 5.76$, $p = 0.001$. $\alpha = 0.025$, days 1–3 and days 4–6). Black bars and asterisks in days 4–6: significant differences between pairs (2-sample t test, $\alpha = 0.0055$).

(B) Imaging CA1PC activity before and after learning while modulating VIP$^+$ IN activity: CA1PCs were imaged on the first and last session with no laser (left – experiment schedule) for mice expressing tdTomato (control, n = 7 mice, first session: 3,668 cells, 524 ± 204 cells/mouse, last session: 3,697 cells, 528 ± 192 cells/mouse, mean ± SD) and ArchT-tdTomato (n = 5 mice, first session: 2,271 cells, 454 ± 166 cells/mouse, last session: 2,204 cells, 441 ± 178 cells/mouse) in VIP$^+$ INs. Right: example FOV with widespread expression of GCaMP6f and ArchT-tdTomato expression in VIP$^+$ INs (red and yellow) in CA1 SP.

(C) CA1PC transient rates (left) and transient AUC (right) were not significantly different between VIP-tdTomato and VIP-ArchT mice in the first and last session (2-way RM ANOVA).

(D) Fraction of place cells (left) and place field width (right) were not significantly different between VIP-tdTomato and VIP-ArchT mice (2-way RM ANOVA).

(E) CA1PC place field distributions for the first (top) and last session (bottom). VIP-tdTomato controls show enrichment of place cells near the reward zone after learning (first session: 1,017 cells, 145 ± 37 cells/mouse, last session: 1,064 cells, 152 ± 54 cells/mouse. VIP-ArchT: first session: 625 cells, 125 ± 41 cells/mouse, last session: 494 cells, 98 ± 31 cells/mouse, mean ± SD).

(legend continued on next page)

firing rates within the reward zone exceeded a set threshold (see STAR Methods). This implementation reproduced GOL-induced place cell enrichment (Figures 8A and 8C, control), similar to experimental observations (Figures 6E and 6F), resulting primarily from recruitment of previously silent place cells. Our model also predicts a locomotion-induced increase in place cell representation of reward location (Figures 8B and 8D). This increase, however, is much smaller than the one induced by learning, corroborating our experimental data (Figure S3D).

To further clarify the role of VIP$^+$ INs during spatial learning, we independently simulated the deletion of each VIP$^+$ IN subtype (VIP$^+$/CR$^+$, VIP$^+$/CCK$^+$) as well as our functionally identified subgroups (VIP-PVM, VIP-NVM). Simulations were performed under three conditions: before learning (Figure 8A, Pre-learning), with learning-related changes in locomotion but no synaptic plasticity (Figure 8B, Locomotion), and after learning the GOL task (locomotion and synaptic plasticity, Figure 8C, Post-learning). In agreement with experimental results, deletion of all VIP$^+$ INs (No VIP) reduced the fraction of CA1PCs encoding reward location post-learning (Figure 8D) and lowered the mean firing rates of CA1PCs (Figure 8E). To investigate whether this effect was primarily mediated by inhibitory (i.e., CCK$^+$) or disinhibitory (i.e., CR$^+$) VIP$^+$ INs, we independently deleted each of these subpopulations in the model circuit. VIP$^+$/CR$^+$ deletion led to a reduction in both the fraction of CA1PC encoding the reward locations (Figure 8D) and the mean firing rates of all modeled place cells, similar to that of removing all VIP$^+$ cells (Figure 8E). In contrast, removal of VIP$^+$/CCK$^+$ cells had no effect on reward encoding (Figure 8D) or the firing rates of CA1PC firing rates (Figure 8E). Respective manipulations of the VIP-PVM and VIP-NVM populations had similar, dampening effects on both enrichment (Figure 8D) and mean CA1PC firing rates (Figure 8E), suggesting similar contributions of these two functional sub-classes of VIP$^+$ INs. These modeling results predict that VIP$^+$ INs affect spatial encoding primarily via their disinhibitory connections onto Basket and Oriens-lacunosum moleculare (OLM) INs (Figure S7). Moreover, in line with the experimental data (Figure S2G), some VIP$^+$ model INs exhibit spatial tuning prior learning (Figure S8). However, the percentage of these VIP$^+$ INs is rather low (~15% in the model, ~29% in experiments), and their tuning is weaker than that of CA1PCs (Figure S2G), suggesting a limited contribution to GOL. Taken together, modeling and experimental results demonstrate that VIP$^+$ IN activity near the reward location plays an active role in goal-directed spatial learning and regulates goal-directed reorganization of hippocampal spatial maps.

DISCUSSION

Prior work has characterized *in vivo* activity patterns of several hippocampal IN types using primarily electrophysiological approaches (Somogyi et al., 2013). However, there is still limited information available regarding *in vivo* activity of VIP$^+$ INs, which comprises the major class of disinhibitory INs in the hippocampus (Acsády et al., 1996a; Chamberland and Topolnik, 2012; Gulyás et al., 1996; Pelkey et al., 2017; Tyan et al., 2014). Our *in vivo* functional imaging study provides the first such characterization of activity profiles of hippocampal VIP$^+$ INs in multiple behavioral settings. Similar to neocortical areas (Fu et al., 2014; Karnani et al., 2016) and other IN types in the hippocampus (Grienberger et al., 2017; Lapray et al., 2012; Varga et al., 2012), including disinhibitory INs located in the CA1 alveus-oriens (Fuhrmann et al., 2015), we found strong locomotion-related activation in the majority of CA1 VIP$^+$ INs. Relatedly, we observed spatial tuning in a subset of CA1 VIP$^+$ INs as has been reported for other IN types (Ego-Stengel and Wilson, 2007; Fuhrmann et al., 2015; Marshall et al., 2002; Wilent and Nitz, 2007) and is replicated by our computational model. However, we also found that a subgroup of hippocampal VIP$^+$ INs responded primarily to the termination of locomotion. This response pattern was largely unobserved in hippocampal PV$^+$ INs but was present in a subset of SOM$^+$ CA1 INs, consistent with previous observations (Arriaga and Han, 2017). In our imaging experiments, we focused on VIP$^+$ INs located in the CA1 pyramidal layer amenable to large-scale imaging. Nevertheless, in future experiments it will be important to carry out a comparative characterization of VIP$^+$ INs located in dendritic layers of CA1 (Chamberland and Topolnik, 2012; Klausberger and Somogyi, 2008; Pelkey et al., 2017). In addition, we note that, although our *in vivo* and *in vitro* optogenetic experiments demonstrate a net disinhibitory influence of VIP$^+$ INs on CA1PC activity in the VIP-IRES-Cre mouse line, INs labeled with this single-marker strategy certainly also include other direct, inhibitory INs; for example, VIP$^+$/CCK$^+$ basket cells. Notably, we tended to observe a higher fraction of NVM cells within the anatomically identified subset of VIP$^+$/CCK$^+$ INs, which might indicate that CCK$^+$ basket cells also play an active role in organizing hippocampal ensemble dynamics during spatial learning (Del Pino et al., 2017; Klausberger et al., 2005).

In addition to locomotion and position signals, we found that VIP$^+$ INs are also modulated by the presence of reward and that this activity strongly depends on task demands: a large population of VIP$^+$ INs exhibited significant task modulation in a GOL task, where the animal learned to associate the reward with a certain spatial location on the treadmill belt. In contrast, behavioral tasks without a learning component recruited smaller task-responsive populations, whose response magnitude was significantly diminished compared to those observed in the goal-oriented task. Further, VIP$^+$ IN activity during the GOL task contained a spatial component associated with the reward location beyond that expected from locomotion and reward-driven responses and could be related to reward anticipation. These results indicate that activity in hippocampal disinhibitory circuits contains a mixture of information about both idiothetic and task variables, where the latter is expressed differentially according to behavioral demands.

(F) Left: fraction of place fields near the reward zone (15% of belt approaching zone) is significantly higher than expected from a uniform distribution of place fields for VIP-tdTomato mice after learning (1-sample t test, $t(6) = 4.43$, $p = 0.004$, $\alpha = 0.0125$). Right: on a per mouse basis, control mice (one-sample t test against a Δfraction of 0, $t(6) = 4.65$, $p = 0.003$, $n = 7$ mice, $\alpha = 0.025$), but not VIP-ArchT mice (1-sample t test, $t(4) = 0.67$, $p = 0.54$, $n = 5$ mice), showed a significant increase in the fraction of place fields near the reward zone post-learning. See also Figures S6 and S7.

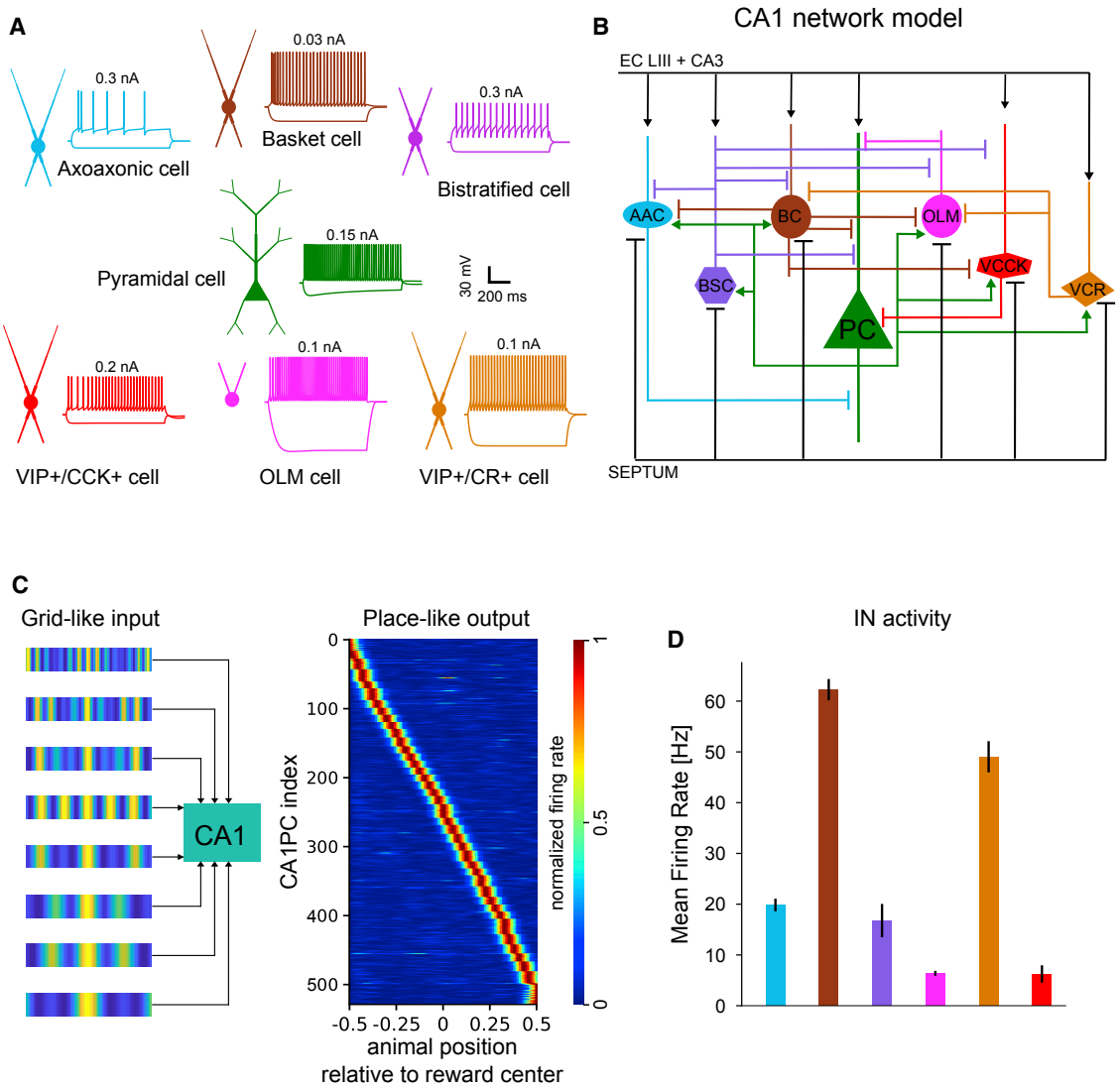

Figure 7. Computational Model of the CA1 Network

(A) Morphological properties of simulated neuronal types and corresponding voltage traces for negative (−0.2 nA) and positive (top of the traces) current injections at the soma (for 1,000 ms).

(B) Schematic diagram of the model connectivity (right). PC, pyramidal cells; AAC, axo-axonic cells; BC, basket cells; BSC, bistratified cells; OLM, Oriens-lacunosum moleculare cells; VCCK, VIP^+/CCK^+ cells; VCR, VIP^+/CR^+ cells.

(C) Left: place cell formation using grid-like inputs. Each pyramidal cell receives an octal of grid-like inputs from entorhinal cortex layer III (EC LIII) and an octal from CA3 pyramidal cells. INs receive inputs from randomly selected EC LIII and CA3 pyramidal cells and inhibitory septal inputs. Right: CA1PC activity before learning (virtual animals cover the track with a constant speed).

(D) Mean firing rate of all INs before learning (mean ± SD). Color scheme is the same as in (A) and (B).

See also Figures S6 and S7.

Our results extend upon previous studies demonstrating that hippocampal GABAergic INs are not static elements of the hippocampal circuitry but rather change their firing activity throughout the course of learning (Dupret et al., 2013; Sheffield et al., 2017; Wilson and McNaughton, 1993). Multi-unit recordings in freely moving rats have demonstrated that changes in the firing rate of CA1 INs correlate either positively or negatively with pyramidal cells' spatial coding as rats learn reward locations, suggesting that INs may actively regulate learning-performance-related reorganization of the hippocampal place map (Dupret et al., 2013). In concert with this observation, here we found that VIP^+ disinhibitory circuits in hippocampal area CA1 also undergo learning-performance-related modulation as mice learn to forage for rewards in a goal-directed spatial learning task. We hypothesize that this enhanced recruitment of hippocampal VIP^+ INs is driven by the dynamics of external reinforcement signals, mirroring observations in auditory and prefrontal cortices (Pi et al., 2013) where disinhibitory circuits are strongly

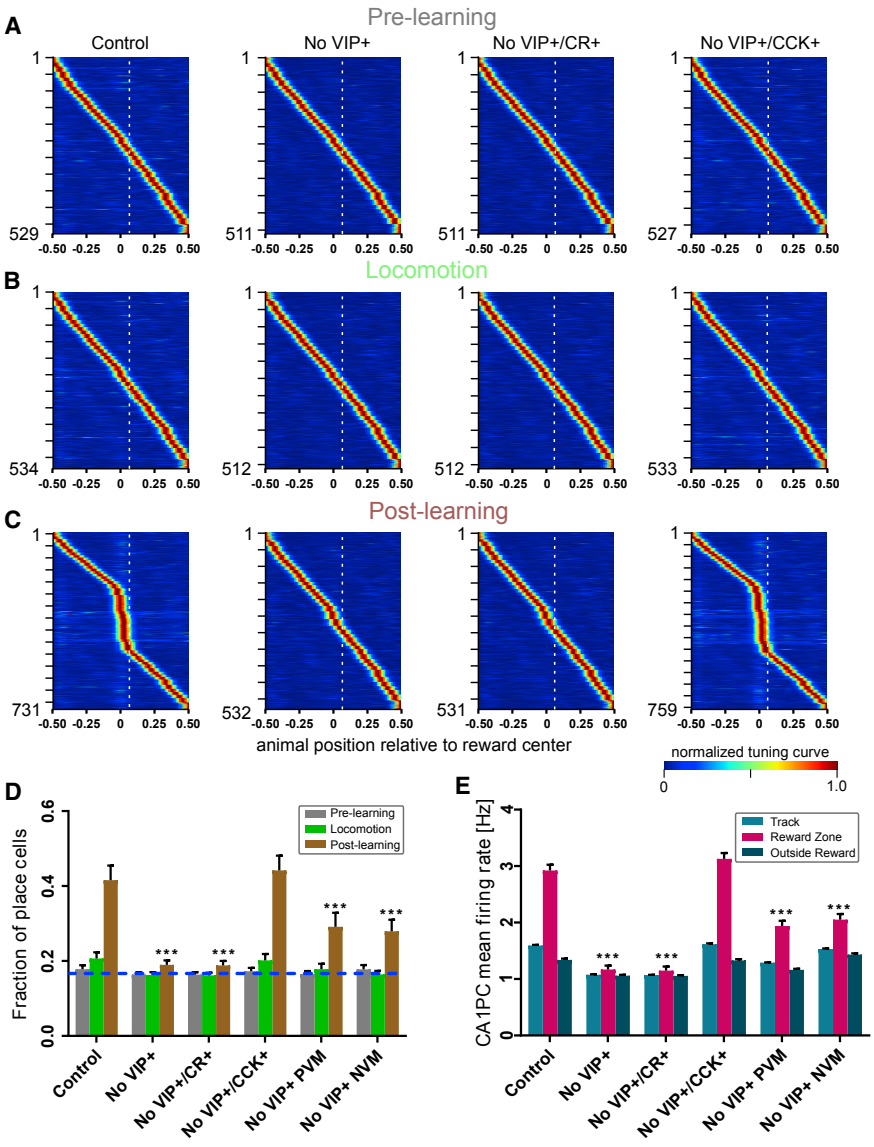

Figure 8. Modeling the Effects of VIP$^+$ INs on Spatial Learning

(A) Spatial heatmaps of CA1PC place cell mean firing rates prior to the simulated GOL learning. Virtual animals cover the 2 m linear track with constant velocity. From left to right: control, deletion of all VIP$^+$ INs, deletion of VIP$^+$/CR$^+$ INs, and deletion of VIP$^+$/CCK$^+$ INs. White dashed line represents the reward location while zero denotes the center of the reward zone.

(B) Same as in (A), with speed modulation. Virtual animals spend more time within the simulated reward zone but no plasticity takes place (similar to day 1 in experiments).

(C) Same as in (A) and (B), after learning the simulated GOL task (similar to day 4 in experiments). Virtual animals spend more time within the simulated reward zone and place cells active in the reward zone have strengthened synaptic weights in their EC and CA3 afferents. The model reproduces the enriched encoding of the reward zone: more CA1PCs have a place field within the reward zone compared to pre-learning (A).

(D) Number of CA1PCs within the reward zone (extending over 15% or 30 cm on the track) under the four deletion conditions (mean ± SEM). Post learning enrichment is significantly decreased when deleting all VIP$^+$ INs and specifically when deleting the VIP$^+$/CR$^+$ population. VIP$^+$/CCK$^+$ deletion has a positive effect on enrichment (comparisons with baseline for all conditions in post-learning stage, 1-sample t test, control: $t(9) = 6.28$, $p = 0.00014$, VIP$^+$ deletion: $t(9) = 1.55$, $p = 0.16$, VIP$^+$/CR$^+$ deletion: $t(9) = 1.65$, $p = 0.13$, VIP$^+$/CCK$^+$ deletion: $t(9) = 7.018$, $p = 0.00006$, VIP$^+$/PVM deletion: $t(9) = 3.49$, $p = 0.007$, VIP$^+$/NVM deletion: $t(9) = 3.61$, $p = 0.0056$, $\alpha = 0.0083$ corrected for 6 comparisons). Differences among groups were statistically significant (2-way ANOVA: learning stage: $F(2, 162) = 80.41$, $p < 10^{-15}$, $\alpha = 0.025$, condition: $F(5, 162) = 14.74$, $p = 6.6 \times 10^{-12}$, $\alpha = 0.01$, interaction: $F(10, 162) = 7.929$, $p = 2.5 \times 10^{-10}$, $\alpha = 0.005$). Removal of VIP$^+$ INs leads to a significant drop in enrichment. This reduction is very similar to the one induced when removing VIP$^+$/CR$^+$ cells, while removal of VIP$^+$/CCK$^+$ cells slightly increases enrichment, comparing with the control respectively. Removal of PVM or NVM VIP$^+$ INs did not have a statistically significant effect on enrichment. Locomotion alone is not sufficient to increase place cell representation of reward location. Stars denote significance with paired t test (two-tailed) with Bonferroni's correction.

(E) Mean CA1PC frequency (mean ± SEM) across the entire track, within the reward zone and outside the reward zone. Place cells have lower firing rates under VIP$^+$ and VIP$^+$/CR$^+$ IN deletion conditions, while removal of VIP$^+$/CCK$^+$ results in not significantly increased firing within the reward zone. Removal of PVM or NVM VIP$^+$ IN also results in similar sized, slightly decreased CA1PC firing (2-way ANOVA: position: $F(2, 11247) = 353.1$, $p < 10^{-15}$, $\alpha = 0.025$, condition: $F(5, 11247) = 147.9$, $p < 10^{-15}$, $\alpha = 0.01$, interaction: $F(10, 11247) = 47.00$, $p < 10^{-15}$, $\alpha = 0.005$). Stars denote significance with unpaired t test (two-tailed) with Bonferroni's correction.

See also Figures S6–S8.

engaged by reinforcement signals to regulate the gain of local principal cell responses. Subcortical neuromodulatory inputs provide an attractive candidate for conveying such a reinforcement signal and have been implicated in signaling reward-related information in the cortex (Hangya et al., 2015; McNamara et al., 2014; Takeuchi et al., 2016). Indeed, we have shown that VIP$^+$ INs receive monosynaptic input from several neuromodulatory centers, including direct connections from cholinergic, serotonergic, and dopaminergic nuclei. This is consistent with our hypothesis that reward-related, external neuromodulatory signals can directly influence the activity of hippocampal VIP$^+$ INs similar to what has been demonstrated for VIP$^+$ INs in neocortical circuits (Alitto and Dan, 2013; Fu et al., 2014; Kuchibhotla et al., 2016; Letzkus et al., 2011, 2015). Future work may permit causal linkage of external inputs to VIP$^+$ IN recruitment in the hippocampus.

Alternatively, it is possible that the performance-related changes we observed in VIP$^+$ IN population dynamics during learning were driven primarily by intrinsic circuit dynamics of CA1. While disinhibition enabled by VIP$^+$ INs could promote the place cell enrichment near reward zones observed during the GOL task (Danielson et al., 2016; Dupret et al., 2010; Gauthier and Tank, 2018; Zaremba et al., 2017), pyramidal cells may directly receive sufficient reinforcement signals to drive this representational shift. Here VIP$^+$ IN circuits could serve to amplify and maintain enhanced pyramidal cell activity at the reward zone through local feedback circuits, in which pyramidal cells provide an enhanced excitatory drive to VIP$^+$ INs, reciprocating further local disinhibition and resulting in a spatially localized reduction in "winner-take-all" dynamics. Our finding that optogenetic activation of VIP$^+$ INs alone is not sufficient to induce place cell remapping would be consistent with this interpretation. The functional clustering of VIP$^+$ INs we observe may derive from differences in feedback connectivity from local pyramidal cells, leading to differences in locomotion responsivity and learning-performance-related dynamics. However, future work will be required to precisely link single-cell functional and molecular heterogeneity in hippocampal disinhibitory circuits and to determine how these are related to the observed dynamics during learning.

Last, we demonstrate that optogenetic manipulation of hippocampal disinhibitory tone can bi-directionally affect spatial learning performance. This parallels observations in prefrontal cortex where optogenetic activation of VIP$^+$ INs enhanced learning performance (Kamigaki and Dan, 2017). Optogenetic suppression of VIP$^+$ INs when the animal was near the reward location impaired learning performance and ablated place cell enrichment. Our genetic strategy is admittedly limited to nonspecific labeling of CA1 VIP$^+$ populations, which includes VIP$^+$/CCK$^+$ INs that directly target CA1PCs. However, these results are consistent with an interpretation that disinhibition provided by VIP$^+$ INs could suppress inhibition to CA1PCs near the reward, thereby facilitating synaptic and intrinsic plasticity in a functional subset of pyramidal cells (Bittner et al., 2015, 2017; Donato et al., 2013; Fu et al., 2015; Grienberger et al., 2017). This may manifest as a structured remapping of place cells toward the reward zone (Danielson et al., 2016; Dupret et al., 2010; Zaremba et al., 2017). We found that optogenetic activation of VIP$^+$ INs alone was not sufficient to induce place cell remapping. This suggests that reward zone-related plasticity of CA1PC place cells requires conjunctive interactions from multiple inputs on CA1PCs, including spatial, sensory, disinhibitory, and neuromodulatory modalities (Bittner et al., 2015).

Disinhibition mediated by VIP$^+$ INs could regulate performance-related reorganization of hippocampal pyramidal cell assemblies during learning through multiple downstream targets. In the neocortex, VIP$^+$ INs primarily innervate SOM$^+$ INs and, to lesser extent, PV$^+$ INs (Kepecs and Fishell, 2014; Lee et al., 2013; Pfeffer et al., 2013; Pi et al., 2013). Efferent targets of hippocampal VIP$^+$ INs are less well characterized likely include multiple different IN types (Acsády et al., 1996a; Donato et al., 2013; Gulyás et al., 1996; Tyan et al., 2014). While our study did not investigate the direct effects of VIP disinhibition on different potential IN targets, disinhibition of either perisomatic or dendrite-targeting INs could play a role in regulating learning-performance-related hippocampal place cell dynamics. For instance, disinhibition through suppressing dendrite-targeting SOM$^+$ IN activity could enhance dendritic electrogenesis and burst firing in pyramidal cells (Lovett-Barron et al., 2014; Royer et al., 2012), facilitating place cell formation and plasticity (Bittner et al., 2015, 2017; Sheffield et al., 2017). Indeed, the negative velocity modulation we observe in a subset of SOM$^+$ INs during RF could arise from inhibition by PVM VIP$^+$ INs. On the other hand, disinhibition of pyramidal cells through suppressing perisomatic targeting PV$^+$ INs (basket and axo-axonic cells) could also enhance network excitability during memory encoding (Donato et al., 2013). The predominant positive velocity modulation we observe for PV$^+$ INs and for the majority of SOM$^+$ INs during RF (Figure S3A) suggests that VIP$^+$ INs modulate, rather than completely suppress activity of their downstream targets. Our model simulations predict an important inhibitory influence of VIP$^+$/CR$^+$ and VIP PVM cells on both SOM$^+$ OLM INs (Figure S7A) and PV$^+$ basket cells (Figure S7B). Moreover, selective removal of specific VIP$^+$/CR$^+$ connections to these INs is shown in the model to dampen enrichment (Figure S7C), suggesting that the VIP$^+$ disinhibitory action on spatial learning is mediated by targeted connections to perisomatic and less to dendrite-targeting INs. Nevertheless, in future studies it will be important to characterize learning-associated changes in the population dynamics of other identified hippocampal INs subtypes (Arriaga and Han, 2017; Caroni, 2015; Dupret et al., 2013; Sheffield et al., 2017) and to dissect the role of VIP$^+$ INs in this process. On the basis of our observations, we propose that the VIP circuit motif of the hippocampal CA1 region, similar to its neocortical counterpart, is a key task-adaptable component of cortical learning mechanisms.

STAR★METHODS

Detailed methods are provided in the online version of this paper and include the following:

- KEY RESOURCES TABLE
- CONTACT FOR REAGENT AND RESOURCE SHARING
- EXPERIMENTAL MODEL AND SUBJECT DETAILS
- METHOD DETAILS
  - Viruses
  - *In vivo* two-photon imaging
  - Simultaneous two-photon imaging and LFP recording
  - Simultaneous two-photon imaging and photostimulation
  - *In vitro* electrophysiology
  - Behavior Tasks
  - Post hoc neurochemical identification of VIP+ INs
  - Immunocytochemical validation of VIP-IRES-Cre mouse line
  - Monosynaptic retrograde rabies tracing
- QUANTIFICATION AND STATISTICAL ANALYSIS
  - Ca^{2+} data preprocessing
  - Signal analysis
  - Statistical analysis
- DATA AND SOFTWARE AVAILABILITY

SUPPLEMENTAL INFORMATION

Supplemental Information includes eight figures and can be found with this article online at https://doi.org/10.1016/j.neuron.2019.01.009.

A video abstract is available at https://doi.org/10.1016/j.neuron.2019.01.009#mmc3.

ACKNOWLEDGMENTS

A.L. is supported by National Institute of Mental Health (NIMH) 1R01MH100631, National Institute of Neurological Disorders and Stroke (NINDS) 1U19NS104590 and 1R01NS094668, the Zegar Family Foundation Award, and the Kavli Foundation. G.F.T. is supported by NYSTEM-C029157 and S10 OD018464. J.O. is supported by NIMH F32MH118716. A.D.G. is supported by the Revson Foundation. B.V.Z. is supported by NINDS U01NS094330 and U01NS099720. P.P., S.C., and I.P. are supported by the ERC Starting Grant dEMORY (ERC-2012-StG-311435).

AUTHOR CONTRIBUTIONS

A.L., G.F.T., and W.-K.L. conceived the project. G.F.T., W.-K.L., and A.L. designed and performed experiments and analyzed the data with the help of J.O., J.B.P., A.D.G., Z.L., M.L., and J.F.Z. B.V.Z. designed and provided reagents. P.P., S.C., and I.P. performed computational modeling. All authors wrote the manuscript.

DECLARATION OF INTERESTS

The authors declare no competing interests.

Received: January 2, 2018
Revised: October 3, 2018
Accepted: December 31, 2018
Published: January 31, 2019

SUPPORTING CITATIONS

The following references appear in the Supplemental Information: Bezaire and Soltesz (2013); Bezaire et al. (2016); Cabral et al. (2014); Cutsuridis et al. (2010); Francavilla et al. (2015); Hok et al. (2007); Konstantoudaki et al. (2014); Kunec et al. (2005); Poirazi et al. (2003); Solstad et al. (2006).

REFERENCES

Acsády, L., Arabadzisz, D., and Freund, T.F. (1996a). Correlated morphological and neurochemical features identify different subsets of vasoactive intestinal polypeptide-immunoreactive interneurons in rat hippocampus. Neuroscience *73*, 299–315.

Acsády, L., Görcs, T.J., and Freund, T.F. (1996b). Different populations of vasoactive intestinal polypeptide-immunoreactive interneurons are specialized to control pyramidal cells or interneurons in the hippocampus. Neuroscience *73*, 317–334.

Alitto, H.J., and Dan, Y. (2013). Cell-type-specific modulation of neocortical activity by basal forebrain input. Front. Syst. Neurosci. *6*, 79.

Allen, W.E., Kauvar, I.V., Chen, M.Z., Richman, E.B., Yang, S.J., Chan, K., Gradinaru, V., Deverman, B.E., Luo, L., and Deisseroth, K. (2017). Global representations of goal-directed behavior in distinct cell types of mouse neocortex. Neuron *94*, 891–907.

Arriaga, M., and Han, E.B. (2017). Dedicated hippocampal inhibitory networks for locomotion and immobility. J. Neurosci. *37*, 9222–9238.

Bezaire, M.J., and Soltesz, I. (2013). Quantitative assessment of CA1 local circuits: Knowledge base for interneuron-pyramidal cell connectivity. Hippocampus *23*, 751–785.

Bezaire, M.J., Raikov, I., Burk, K., Vyas, D., and Soltesz, I. (2016). Interneuronal mechanisms of hippocampal theta oscillations in a full-scale model of the rodent CA1 circuit. eLife *5*, 5.

Bittner, K.C., Grienberger, C., Vaidya, S.P., Milstein, A.D., Macklin, J.J., Suh, J., Tonegawa, S., and Magee, J.C. (2015). Conjunctive input processing drives feature selectivity in hippocampal CA1 neurons. Nat. Neurosci. *18*, 1133–1142.

Bittner, K.C., Milstein, A.D., Grienberger, C., Romani, S., and Magee, J.C. (2017). Behavioral time scale synaptic plasticity underlies CA1 place fields. Science *357*, 1033–1036.

Cabral, H.O., Fouquet, C., Rondi-Reig, L., Pennartz, C.M., and Battaglia, F.P. (2014). Single-trial properties of place cells in control and CA1 NMDA receptor subunit 1-KO mice. J. Neurosci. *34*, 15861–15869.

Caroni, P. (2015). Inhibitory microcircuit modules in hippocampal learning. Curr. Opin. Neurobiol. *35*, 66–73.

Cea-del Rio, C.A., Lawrence, J.J., Tricoire, L., Erdelyi, F., Szabo, G., and McBain, C.J. (2010). M3 muscarinic acetylcholine receptor expression confers differential cholinergic modulation to neurochemically distinct hippocampal basket cell subtypes. J. Neurosci. *30*, 6011–6024.

Chamberland, S., and Topolnik, L. (2012). Inhibitory control of hippocampal inhibitory neurons. Front. Neurosci. *6*, 165.

Cutsuridis, V., Cobb, S., and Graham, B.P. (2010). Encoding and retrieval in a model of the hippocampal CA1 microcircuit. Hippocampus *20*, 423–446.

Danielson, N.B., Zaremba, J.D., Kaifosh, P., Bowler, J., Ladow, M., and Losonczy, A. (2016). Sublayer-specific coding dynamics during spatial navigation and learning in hippocampal area CA1. Neuron *91*, 652–665.

Dávid, C., Schleicher, A., Zuschratter, W., and Staiger, J.F. (2007). The innervation of parvalbumin-containing interneurons by VIP-immunopositive interneurons in the primary somatosensory cortex of the adult rat. Eur. J. Neurosci. *25*, 2329–2340.

Del Pino, I., Brotons-Mas, J.R., Marques-Smith, A., Marighetto, A., Frick, A., Marín, O., and Rico, B. (2017). Abnormal wiring of CCK^+ basket cells disrupts spatial information coding. Nat. Neurosci. *20*, 784–792.

Dombeck, D.A., Khabbaz, A.N., Collman, F., Adelman, T.L., and Tank, D.W. (2007). Imaging large-scale neural activity with cellular resolution in awake, mobile mice. Neuron *56*, 43–57.

Dombeck, D.A., Harvey, C.D., Tian, L., Looger, L.L., and Tank, D.W. (2010). Functional imaging of hippocampal place cells at cellular resolution during virtual navigation. Nat. Neurosci. *13*, 1433–1440.

Donato, F., Rompani, S.B., and Caroni, P. (2013). Parvalbumin-expressing basket-cell network plasticity induced by experience regulates adult learning. Nature *504*, 272–276.

Dupret, D., O'Neill, J., Pleydell-Bouverie, B., and Csicsvari, J. (2010). The reorganization and reactivation of hippocampal maps predict spatial memory performance. Nat. Neurosci. *13*, 995–1002.

Dupret, D., O'Neill, J., and Csicsvari, J. (2013). Dynamic reconfiguration of hippocampal interneuron circuits during spatial learning. Neuron *78*, 166–180.

Ego-Stengel, V., and Wilson, M.A. (2007). Spatial selectivity and theta phase precession in CA1 interneurons. Hippocampus *17*, 161–174.

Eichenbaum, H. (2000). A cortical-hippocampal system for declarative memory. Nat. Rev. Neurosci. *1*, 41–50.

Fishell, G., and Rudy, B. (2011). Mechanisms of inhibition within the telencephalon: "Where the wild things are". Annu. Rev. Neurosci. *34*, 535–567.

Francavilla, R., Luo, X., Magnin, E., Tyan, L., and Topolnik, L. (2015). Coordination of dendritic inhibition through local disinhibitory circuits. Front. Synaptic Neurosci. *7*, 5.

Freund, T.F., and Buzsáki, G. (1996). Interneurons of the hippocampus. Hippocampus *6*, 347–470.

Fu, Y., Tucciarone, J.M., Espinosa, J.S., Sheng, N., Darcy, D.P., Nicoll, R.A., Huang, Z.J., and Stryker, M.P. (2014). A cortical circuit for gain control by behavioral state. Cell *156*, 1139–1152.

Fu, Y., Kaneko, M., Tang, Y., Alvarez-Buylla, A., and Stryker, M.P. (2015). A cortical disinhibitory circuit for enhancing adult plasticity. eLife *4*, e05558.

Fuhrmann, F., Justus, D., Sosulina, L., Kaneko, H., Beutel, T., Friedrichs, D., Schoch, S., Schwarz, M.K., Fuhrmann, M., and Remy, S. (2015). Locomotion,

theta oscillations, and the speed-correlated firing of hippocampal neurons are controlled by a medial septal glutamatergic circuit. Neuron *86*, 1253–1264.

Gauthier, J.L., and Tank, D.W. (2018). A dedicated population for reward coding in the hippocampus. Neuron *99*, 179–193.

Grienberger, C., Milstein, A.D., Bittner, K.C., Romani, S., and Magee, J.C. (2017). Inhibitory suppression of heterogeneously tuned excitation enhances spatial coding in CA1 place cells. Nat. Neurosci. *20*, 417–426.

Gulyás, A.I., Hájos, N., and Freund, T.F. (1996). Interneurons containing calretinin are specialized to control other interneurons in the rat hippocampus. J. Neurosci. *16*, 3397–3411.

Hangya, B., Ranade, S.P., Lorenc, M., and Kepecs, A. (2015). Central cholinergic neurons are rapidly recruited by reinforcement feedback. Cell *162*, 1155–1168.

Harris, K.D., Csicsvari, J., Hirase, H., Dragoi, G., and Buzsáki, G. (2003). Organization of cell assemblies in the hippocampus. Nature *424*, 552–556.

Hines, M.L., and Carnevale, N.T. (1997). The NEURON simulation environment. Neural Comput. *9*, 1179–1209.

Hok, V., Lenck-Santini, P.P., Roux, S., Save, E., Muller, R.U., and Poucet, B. (2007). Goal-related activity in hippocampal place cells. J. Neurosci. *27*, 472–482.

Jia, H., Rochefort, N.L., Chen, X., and Konnerth, A. (2011). In vivo two-photon imaging of sensory-evoked dendritic calcium signals in cortical neurons. Nat. Protoc. *6*, 28–35.

Kaifosh, P., Zaremba, J.D., Danielson, N.B., and Losonczy, A. (2014). SIMA: Python software for analysis of dynamic fluorescence imaging data. Front. Neuroinform. *8*, 80.

Kamigaki, T., and Dan, Y. (2017). Delay activity of specific prefrontal interneuron subtypes modulates memory-guided behavior. Nat. Neurosci. *20*, 854–863.

Karnani, M.M., Jackson, J., Ayzenshtat, I., Hamzehei Sichani, A., Manoocheri, K., Kim, S., and Yuste, R. (2016). Opening holes in the blanket of inhibition: Localized lateral disinhibition by VIP interneurons. J. Neurosci. *36*, 3471–3480.

Keemink, S.W., Lowe, S.C., Pakan, J.M.P., Dylda, E., van Rossum, M.C.W., and Rochefort, N.L. (2018). FISSA: A neuropil decontamination toolbox for calcium imaging signals. Sci. Rep. *8*, 3493.

Kepecs, A., and Fishell, G. (2014). Interneuron cell types are fit to function. Nature *505*, 318–326.

Klausberger, T., and Somogyi, P. (2008). Neuronal diversity and temporal dynamics: The unity of hippocampal circuit operations. Science *321*, 53–57.

Klausberger, T., Marton, L.F., O'Neill, J., Huck, J.H., Dalezios, Y., Fuentealba, P., Suen, W.Y., Papp, E., Kaneko, T., Watanabe, M., et al. (2005). Complementary roles of cholecystokinin- and parvalbumin-expressing GABAergic neurons in hippocampal network oscillations. J. Neurosci. *25*, 9782–9793.

Konstantoudaki, X., Papoutsi, A., Chalkiadaki, K., Poirazi, P., and Sidiropoulou, K. (2014). Modulatory effects of inhibition on persistent activity in a cortical microcircuit model. Front. Neural Circuits *8*, 7.

Kuchibhotla, K.V., Gill, J.V., Lindsay, G.W., Papadoyannis, E.S., Field, R.E., Sten, T.A., Miller, K.D., and Froemke, R.C. (2016). Parallel processing by cortical inhibition enables context-dependent behavior. Nat. Neurosci. *20*, 62–71.

Kunec, S., Hasselmo, M.E., and Kopell, N. (2005). Encoding and retrieval in the CA3 region of the hippocampus: A model of theta-phase separation. J. Neurophysiol. *94*, 70–82.

Lapray, D., Lasztoczi, B., Lagler, M., Viney, T.J., Katona, L., Valenti, O., Hartwich, K., Borhegyi, Z., Somogyi, P., and Klausberger, T. (2012). Behavior-dependent specialization of identified hippocampal interneurons. Nat. Neurosci. *15*, 1265–1271.

Lee, S., Kruglikov, I., Huang, Z.J., Fishell, G., and Rudy, B. (2013). A disinhibitory circuit mediates motor integration in the somatosensory cortex. Nat. Neurosci. *16*, 1662–1670.

Letzkus, J.J., Wolff, S.B., Meyer, E.M., Tovote, P., Courtin, J., Herry, C., and Lüthi, A. (2011). A disinhibitory microcircuit for associative fear learning in the auditory cortex. Nature *480*, 331–335.

Letzkus, J.J., Wolff, S.B., and Lüthi, A. (2015). Disinhibition, a circuit mechanism for associative learning and memory. Neuron *88*, 264–276.

Lovett-Barron, M., Kaifosh, P., Kheirbek, M.A., Danielson, N., Zaremba, J.D., Reardon, T.R., Turi, G.F., Hen, R., Zemelman, B.V., and Losonczy, A. (2014). Dendritic inhibition in the hippocampus supports fear learning. Science *343*, 857–863.

Marshall, L., Henze, D.A., Hirase, H., Leinekugel, X., Dragoi, G., and Buzsáki, G. (2002). Hippocampal pyramidal cell-interneuron spike transmission is frequency dependent and responsible for place modulation of interneuron discharge. J. Neurosci. *22*, RC197.

McNamara, C.G., Tejero-Cantero, Á., Trouche, S., Campo-Urriza, N., and Dupret, D. (2014). Dopaminergic neurons promote hippocampal reactivation and spatial memory persistence. Nat. Neurosci. *17*, 1658–1660.

Nathanson, J.L., Yanagawa, Y., Obata, K., and Callaway, E.M. (2009). Preferential labeling of inhibitory and excitatory cortical neurons by endogenous tropism of adeno-associated virus and lentivirus vectors. Neuroscience *161*, 441–450.

O'Keefe, J., and Dostrovsky, J. (1971). The hippocampus as a spatial map. Preliminary evidence from unit activity in the freely-moving rat. Brain Res. *34*, 171–175.

Paxinos, G., and Franklin, K.B.J. (2004). The Mouse Brain in Stereotaxic Coordinates, Second Edition (Academic Press).

Pedregosa, F., Varoquaux, G., Gramfort, A., Michel, V., Thirion, B., Grisel, O., Blondel, M., Prettenhofer, P., Weiss, R., Dubourg, V., et al. (2011). Scikit-learn: Machine learning in Python. J. Mach. Learn. Res. *12*, 2825–2830.

Pelkey, K.A., Chittajallu, R., Craig, M.T., Tricoire, L., Wester, J.C., and McBain, C.J. (2017). Hippocampal GABAergic Inhibitory Interneurons. Physiol. Rev. *97*, 1619–1747.

Pfeffer, C.K., Xue, M., He, M., Huang, Z.J., and Scanziani, M. (2013). Inhibition of inhibition in visual cortex: The logic of connections between molecularly distinct interneurons. Nat. Neurosci. *16*, 1068–1076.

Pi, H.J., Hangya, B., Kvitsiani, D., Sanders, J.I., Huang, Z.J., and Kepecs, A. (2013). Cortical interneurons that specialize in disinhibitory control. Nature *503*, 521–524.

Pinto, L., and Dan, Y. (2015). Cell-type-specific activity in prefrontal cortex during goal-directed behavior. Neuron *87*, 437–450.

Poirazi, P., Brannon, T., and Mel, B.W. (2003). Arithmetic of subthreshold synaptic summation in a model CA1 pyramidal cell. Neuron *37*, 977–987.

Rajasethupathy, P., Sankaran, S., Marshel, J.H., Kim, C.K., Ferenczi, E., Lee, S.Y., Berndt, A., Ramakrishnan, C., Jaffe, A., Lo, M., et al. (2015). Projections from neocortex mediate top-down control of memory retrieval. Nature *526*, 653–659.

Reardon, T.R., Murray, A.J., Turi, G.F., Wirblich, C., Croce, K.R., Schnell, M.J., Jessell, T.M., and Losonczy, A. (2016). Rabies virus CVS-N2c(ΔG) strain enhances retrograde synaptic transfer and neuronal viability. Neuron *89*, 711–724.

Royer, S., Zemelman, B.V., Losonczy, A., Kim, J., Chance, F., Magee, J.C., and Buzsáki, G. (2012). Control of timing, rate and bursts of hippocampal place cells by dendritic and somatic inhibition. Nat. Neurosci. *15*, 769–775.

Scheyltjens, I., Laramée, M.E., Van den Haute, C., Gijsbers, R., Debyser, Z., Baekelandt, V., Vreysen, S., and Arckens, L. (2015). Evaluation of the expression pattern of rAAV2/1, 2/5, 2/7, 2/8, and 2/9 serotypes with different promoters in the mouse visual cortex. J. Comp. Neurol. *523*, 2019–2042.

Schoenenberger, P., O'Neill, J., and Csicsvari, J. (2016). Activity-dependent plasticity of hippocampal place maps. Nat. Commun. *7*, 11824.

Sheffield, M.E.J., Adoff, M.D., and Dombeck, D.A. (2017). Increased prevalence of calcium transients across the dendritic arbor during place field formation. Neuron *96*, 490–504.

Skaggs, W.E., Mcnaughton, B.L., Markus, E.J., and Gothard, K.M. (1993). An information-theoretic approach to deciphering the hippocampal code. Adv. Neural Inf. Process. Syst. *5*, 1030–1037.

Solstad, T., Moser, E.I., and Einevoll, G.T. (2006). From grid cells to place cells: A mathematical model. Hippocampus *16*, 1026–1031.

Somogyi, J., Baude, A., Omori, Y., Shimizu, H., El Mestikawy, S., Fukaya, M., Shigemoto, R., Watanabe, M., and Somogyi, P. (2004). GABAergic basket cells expressing cholecystokinin contain vesicular glutamate transporter type 3 (VGLUT3) in their synaptic terminals in hippocampus and isocortex of the rat. Eur. J. Neurosci. *19*, 552–569.

Somogyi, P., Katona, L., Klausberger, T., Lasztóczi, B., and Viney, T.J. (2013). Temporal redistribution of inhibition over neuronal subcellular domains underlies state-dependent rhythmic change of excitability in the hippocampus. Philos. Trans. R. Soc. Lond. B Biol. Sci. *369*, 20120518.

Takeuchi, T., Duszkiewicz, A.J., Sonneborn, A., Spooner, P.A., Yamasaki, M., Watanabe, M., Smith, C.C., Fernández, G., Deisseroth, K., Greene, R.W., and Morris, R.G. (2016). Locus coeruleus and dopaminergic consolidation of everyday memory. Nature *537*, 357–362.

Tyan, L., Chamberland, S., Magnin, E., Camiré, O., Francavilla, R., David, L.S., Deisseroth, K., and Topolnik, L. (2014). Dendritic inhibition provided by interneuron-specific cells controls the firing rate and timing of the hippocampal feedback inhibitory circuitry. J. Neurosci. *34*, 4534–4547.

Varga, C., Golshani, P., and Soltesz, I. (2012). Frequency-invariant temporal ordering of interneuronal discharges during hippocampal oscillations in awake mice. Proc. Natl. Acad. Sci. USA *109*, E2726–E2734.

Wilent, W.B., and Nitz, D.A. (2007). Discrete place fields of hippocampal formation interneurons. J. Neurophysiol. *97*, 4152–4161.

Wilson, M.A., and McNaughton, B.L. (1993). Dynamics of the hippocampal ensemble code for space. Science *261*, 1055–1058.

Zaremba, J.D., Diamantopoulou, A., Danielson, N.B., Grosmark, A.D., Kaifosh, P.W., Bowler, J.C., Liao, Z., Sparks, F.T., Gogos, J.A., and Losonczy, A. (2017). Impaired hippocampal place cell dynamics in a mouse model of the 22q11.2 deletion. Nat. Neurosci. *20*, 1612–1623.

Zhang, S., Xu, M., Kamigaki, T., Hoang Do, J.P., Chang, W.C., Jenvay, S., Miyamichi, K., Luo, L., and Dan, Y. (2014). Selective attention. Long-range and local circuits for top-down modulation of visual cortex processing. Science *345*, 660–665.

STAR★METHODS

KEY RESOURCES TABLE

REAGENT or RESOURCE	SOURCE	IDENTIFIER
Antibodies		
Chicken anti-GFP	abcam	ab13970
Rabbit anti-pro-Cholecystokinin	Frontier Institute	CCK-pro-Rb-Af350
Mouse anti-Calretinin	Swant	6B3
Donkey anti-chicken-AlexaFluor488	Jackson ImmunoResearch	703-545-155
Donkey anti-rabbit-DyLight405	Jackson ImmunoResearch	711-475-152
Donkey anti-rabbit-AlexaFluor594	Jackson ImmunoResearch	711-585-152
Donkey a-mouse-DyLight649	Jackson ImmunoResearch	715-605-151
Rabbit anti-VIP	Immunostar	20077
Goat anti-RFP	Rockland	200-101-379
Avidine-Cy5	Molecular probes	SA1011
Rabbit anti-HA tag	abcam	ab20084
Donkey anti-Goat Alexa 594	Jackson ImmunoResearch	705-585-147
Bacterial and Virus Strains		
rAAV2/1:EF1α-(GCaMP6f)^{Cre}	Boris Zemelman	N/A
rAAV2/1:Syn-(ArchT-tdTomato)^{Cre}	Boris Zemelman	N/A
rAAV2/1:Syn-(ChR2-GFP)^{Cre}	Boris Zemelman	N/A
rAAV2/1:Syn-(GFP)^{Cre}	Boris Zemelman	N/A
rAAV2/1:Syn-(tdTomato)^{Cre}	Boris Zemelman	N/A
rAAV2/1:CaMKII-GCaMP6f	Boris Zemelman	N/A
rAAV2/9:EF1α-(bReaChES-tdTomato)^{Cre}	Boris Zemelman	N/A
rAAV2/1:EF1α-(ArchT-tdTomato)^{Cre}	Boris Zemelman	N/A
AAV2/1:EF1α-(TVA-mCherry)^{Cre}	Univ. North Carolina Vector Core	N/A
AAV2/1-pAM-CAGGS:H2B-(3XHA-P2A-N2cG)^{Cre}	Reardon et al., 2016	N/A
ENVA-CVS-N2c$^{\Delta G}$	Reardon et al., 2016	N/A
Chemicals, Peptides, and Recombinant Proteins		
TSA Kit	Molecular Probes	T20921
Deposited Data		
Analyzed data	This paper	N/A
CA1 network model	This paper	N/A
Experimental Models: Organisms/Strains		
B6;129S6-Gt(ROSA)26Sor$^{tm9(CAG-tdTomato)Hze/J}$	The Jackson Laboratory	007905
VIP-IRES-cre	The Jackson Laboratory	010908
Pvalb-IRES-Cre	Lovett-Barron et al., 2014	N/A
Som-IRES-Cre	Lovett-Barron et al., 2014	N/A
Software and Algorithms		
Prism 8.00	GraphPad	N/A
Python 2.7.15	https://www.python.org/	N/A
SIMA	Kaifosh et al., 2014	https://github.com/losonczylab/sima
NEURON v7.5	Hines and Carnevale, 1997	N/A
FISSA	Keemink et al., 2018	https://github.com/rochefort-lab/fissa

CONTACT FOR REAGENT AND RESOURCE SHARING

Further information and requests for resources and reagents should be directed to and will be fulfilled by the Lead Contact, Attila Losonczy (al2856@columbia.edu).

EXPERIMENTAL MODEL AND SUBJECT DETAILS

All experiments were conducted in accordance with the NIH guidelines and with the approval of the Columbia University Institutional Animal Care and Use Committee. Experiments were performed with healthy adult, heterozygous male and female VIP-IRES-Cre mice (Jackson Laboratory, Stock No: 010908) crossed with C57/Bl6 mice or with the Cre-dependent tdTomato reporter line (Jackson Laboratory, Stock No: 007909; B6;129S6-Gt(ROSA)26Sor$^{tm9(CAG-tdTomato)Hze/J}$, Ai9). For comparing VIP+ INs activity with PV+ and SOM+ INs, we used heterozygous male and female Pvalb-IRES-Cre and Som-IRES-Cre knock-in mice generated by Dr. Boris Zemelman (Lovett-Barron et al., 2014). Mice were kept in the vivarium on a reversed 12-h light/dark cycle and were housed 3-5 mice in each cage. Experiments were performed during the dark portion of the cycle.

METHOD DETAILS

Viruses

Cre-dependent recombinant adeno-associated virus (rAAV) expressing GCaMP6f under the EF1α promoter (rAAV2/1:EF1α-(GCaMP6f)^{Cre}), was used for expressing GCaMP6f in VIP+ INs for imaging experiments (Figures 2, 3, 4, 5, S1C, S1D, and S2C–S2G) and for imaging PV+ and SOM+ INs (Figure S3). For *in vitro* electrophysiological recordings (Figure 1B) VIP-IRES-Cre mice were injected with rAAV2/1:Syn-(ArchT-tdTomato)^{Cre} in the dorsal CA1. For optogenetic manipulation of VIP+ INs during the head-fixed GOL task (Figure 6A), mice were injected bilaterally in the dorsal hippocampal area CA1 with rAAV2/1:Syn-(ChR2-GFP)^{Cre} or rAAV2/1:Syn-(ArchT-tdTomato)^{Cre} viruses and rAAV2/1:Syn-(GFP)^{Cre} or rAAV2/1:Syn-(tdTomato)^{Cre} as controls, respectively. To simultaneously image CA1 pyramidal cells and manipulate VIP+ INs (Figure 1) we injected mice unilaterally with a 1:1 mixture of rAAV2/1:CaMKII-GCaMP6f and rAAV2/1:Syn-(ArchT-tdTomato)^{Cre} (Figures S2A and S2B) or with a 1:1 mixture of rAAV2/9:EF1α-(bReaChES-tdTomato)^{Cre} (Rajasethupathy et al., 2015) and rAAV2/1:CaMKII-GCaMP6f virus (Figures 1C and 1D). Consistent with the reported limited specificity of the CaMKII rAAV promoter to label selectively excitatory neurons (Nathanson et al., 2009; Scheyltjens et al., 2015; Schoenenberger et al., 2016), we observed that the CaMKII promoter-driven rAAV led to GCaMP expression in both pyramidal cells and interneurons. Therefore, VIP+ INs were identified based on their Cre-dependent tdTomato expression.

Viral injection, hippocampal window implant and head-fixed optogenetic manipulations

Viral injection and imaging window implant procedures are described in details elsewhere (Danielson et al., 2016; Lovett-Barron et al., 2014). Briefly, viruses were stereotactically injected into the dorsal CA1 (coordinates relative to Bregma: anterio-posterior −2.2, medio-lateral 1.6, dorso-ventral: −1.2, −1.1, −1.0) of adult mice using thin glass pipettes (20-30 nL virus at each dorsoventral spot) and Nanoject II injectors (Drummond Scientific). Mice were returned to their home cage for 3 days before window implantation. After the recovery period mice were surgically implanted with an imaging window (diameter, 3.0 mm; height, 1.5 mm) over the left dorso-intermediate hippocampus and with a stainless-steel head-post for head fixation during imaging. Imaging cannulas were constructed by adhering (Norland optical adhesive) a 3-mm glass coverslip (64-0720, Warner) to a cylindrical steel cannula.

For head-fixed optogenetic manipulations we used published techniques (Lovett-Barron et al., 2014) for the construction of chronically dwelling optical fibers and patch cables for optogenetic behavioral procedures (Thorlabs). For all experiments, a 200 μm core, 0.37 numerical aperture (NA) multimode fiber was used (Thorlabs) for optical stimulation via a patch cable (Thorlabs) connected to either a 100 mw 593.5 or 473 nm laser diode (CrystaLaser) to activate ArchT or ChR2, respectively (laser power was set to 20 mW measured at the tip of the fiber: ~634 mW/mm^2). Adult mice were surgically implanted bilaterally with fiber optic cannulas using published protocols (Lovett-Barron et al., 2014) over the dorsal hippocampal CA1. The positioning of the ferrules and the expression of the opsins were verified post hoc following the end of the recording sessions (Figure S5A).

In vivo two-photon imaging

All imaging was conducted using a two-photon microscope equipped with an 8 kHz resonant scanner (Bruker). For excitation, we used 50-100 mW laser power under the objective (Chameleon Ultra II, Coherent or Insight X3, Spectra Physics tuned to 920 nm or 940 nm, respectively). Red (tdTomato) and green (GCaMP6f) channels were separated by an emission cube set (green, HQ525/70 m-2p; red, HQ607/45 m-2p; 575dcxr, Chroma Technology), and fluorescence signals were collected with photomultiplier tubes (GCaMP fluorescence, GaAsP PMT, Hamamatsu Model 7422P-40). A custom dual stage preamp (1.43105 dB, Bruker) was used to amplify signals prior to digitization. For the consecutive imaging and optogenetic manipulation and Ca^{2+} recording in Figures 6 and S5C we imaged the mice in the first running session and then we placed a laser (593 nm) coupled optical fiber above the hippocampal window in the consecutive 7 running sessions. Finally, we imaged the mice again in the last (9th) session without the laser.

Simultaneous two-photon imaging and LFP recording

To image VIP+ INs' Ca^{2+} activity and correlate it with LFP, we first injected mice with rAAV2/1:EF1α-GCaMP6f in the left dorsal hippocampus. We then implanted mice with hippocampal imaging windows over the left injected area and inserted a chronic, 4-site silicon probe (Qtrode, Neuronexus) in the contralateral CA1 at a 45° angle (coordinates: antero-posterior: −2.3 mm, mediolateral: 2.75 mm, dorsoventral: −0.975 mm). We secured the probe in place with dental acrylic and let the mouse recover for 3 days before the start of training. LFP signals were recorded with a multichannel recording system (Intan Technologies) synchronized with the two-photon microscope. The correct position of the recording electrode was verified by the presence of sharp-wave ripple events in the traces and in some cases with histology. LFP signals were recorded at 25 kHz and down sampled to 1250 Hz.

Simultaneous two-photon imaging and photostimulation

In order to validate the disinhibitory effect of VIP+ INs on CA1 pyramidal cells (Figure 1C), and to assess the effect of VIP+ IN activation on CA1 place cell dynamics in the absence of reward (Figure 5C) we carried out simultaneous Ca^{2+} imaging and photostimulation experiments where we used 620 nm light to excite opsin expressing neurons delivered via an LED coupled to the 2-photon microscope. For optogenetic activation of VIP+ INs, we injected VIP-IRES-Cre mice in dorsal CA1 with a 1:1 mixture of rAAV2/9:EF1α-(bReaChES-tdTomato)^{Cre} and rAAV2/1:CaMKII-GCaMP6f virus. To inhibit VIP+ INs, we injected VIP-IRES-Cre mice in dorsal CA1 with a 1:1 mixture of rAAV2/1:Syn-(ArchT-tdTomato)^{Cre} and rAAV2/1:CaMKII-GCaMP6f viruses. This labeling strategy resulted in pyramidal cells expressing only GCaMP6f while VIP+ cells expressed both GCaMP6f and the opsin. Control mice groups were injected with a 1:1 mixture of rAAV2/1:Syn-(tdTomato)^{Cre} and rAAV2/1:CaMKII-GCaMP6f viruses. To avoid saturating the PMTs during recording sessions when the opsins were activated, we used a fast response time LED (Prizmatix, 620 nm) and custom-made electronics to trigger light pulses on the fly back time of the galvanometer when there is no image acquisition. The average power of the LED was 10-20 mW measured under the objective. This approach allowed us to protect our PMTs from the high intensity illumination but still take the advantage of the fast, full frame resonant galvo scanning without losing any frames during photostimulation.

In vitro electrophysiology

Solutions

Transcardial perfusions, hippocampal microdissections, and sectioning were carried out using ice-cold dissection solution containing 195 mM sucrose, 10 mM NaCl, 15 mM dextrose, 26 mM $NaHCO_3$, 2.5 mM KCl, 1.25 mM NaH_2PO_4, 1 mM $CaCl_2$, 2 mM $MgCl_2 \cdot 6H_2O$. During recordings, slices were continuously perfused at 32°C with ACSF containing 125 mM NaCl, 10 mM dextrose, 26 mM $NaHCO_3$, 2.5 mM KCl, 1.25 mM NaH_2PO_4, 2 mM Na-pyruvate, 2 mM $CaCl_2$, 1 mM $MgCl_2 \cdot 6H_2O$. Dissection solution and ACSF were carbogenated to saturation at all times and were calibrated to pH 7.3-7.4 and osmolality 310 ± 5 mOsm. Whole cell current clamp recordings were performed using a K-gluconate-based internal solution (130 mM K-gluconate, 8 mM KCl, 10 mM HEPES, 4 mM NaCl, 4 mM Mg2ATP, 0.3 mM Tris2GTP, 14 mM (tris-)phosphocreatine) with pH = 7.28 and osmolality 295 mOsm.

Acute slice preparation

2-4 weeks after viral injection of rAAV2/1:EF1α-(ArchT-tdTomato)^{Cre} in dorsal CA1 of VIP-IRES-Cre mice, (8-10 week old) animals were transcardially perfused with ice-cold, carbogenated high-sucrose dissection solution under continuous isoflurane anesthesia (3%–5% induction, 2% maintenance). Brains were quickly removed and placed in ice-cold dissection solution where hippocampi were dissected out, embedded in 4% agar blocks, and sliced in the same solution using a Leica VT1200S vibratome for 400 μm-thick transverse sections. Slices recovered in ACSF at 32°C for 20-30 min and were then held at room temperature until used for recording.

Electrophysiological recordings

Whole-cell current clamp recordings were carried out at 32°C in ACSF using borosilicate glass pipettes. Data were acquired using a MultiClamp 700B amplifier and Digidata 1440A digitizer (Molecular Devices). Data were digitized at 50 kHz and low-pass filtered at 1 kHz. Because measurements were made within-cell, experimental factors such as series resistance and whole cell capacitance were not compensated. While recording pyramidal cells in ArchT-expressing slices, Schaffer collateral fibers were stimulated in stratum radiatum by a glass pipet filled with 1 mM NaCl. Stimuli were delivered across a range of increasing intensities (7 sweeps per intensity) while a 532 nm laser (Opto Engine) was triggered on every other sweep to deliver green light through a ferrule submerged in the perfusion chamber. Laser onset preceded electrical stimulation by 50 ms and lasted for the duration of the pyramidal cell response. Mild positive holding current was sometimes used to hold pyramidal cells between −58 and −65 mV to improve visibility of IPSPs.

Whole cell electrophysiological recordings

To assess evoked inhibition onto pyramidal cells, the IPSP was bracketed in time and integrated with respect to baseline membrane potential. For each recording, laser effect was measured separately for each stimulation intensity by calculating the mean IPSP integral from three laser-OFF and three laser-ON sweeps. To avoid a systematic bias due to order of testing, analysis alternately began on the first or second of 7 trials for each intensity, i.e., starting the analysis with laser off versus on. Analyses were carried out in MATLAB (Mathworks).

Behavior Tasks

Head-fixed mice ran on a 2-m long treadmill belt equipped with a water delivery port and custom made electronics required for recording the mice's licking and its position on the belt. We started to habituate the mice to the head-fixed condition 3-4 days after the head-post implant procedure. Water deprived mice were trained to run on a cue-less belt to run and seek reward by licking the lick

port. The training period typically lasted for 10-14 days or until the mice were able to run reliably for at least 10 laps in 10 min while licking continuously for reward. In imaging experiments for measuring the disinhibitory effect of VIP+ IN activation (Figure 1C), the optogenetics LED was triggered on alternating laps for 40% (80cm) of the lap around a fixed position. For RF, animals ran on the belt and water rewards were delivered randomly (without requiring the animal to lick the lick port to solicit the reward) on either a cued belt (Figures 2, 3, 4, and S5B). Animals performed this task for 3x10 minute sessions per day for either two days (Figure 2) or 3 days (Figure S5B). For the goal oriented learning task (GOL, Figures 3 and 6), animals learned to seek reward at a fixed location on a cued belt. The cued belt is composed of 3 segments of fabric of different texture and with many tactile cues glued/sewed to the belt at different positions on the belt. The cues have different texture properties and different heights that let the animal sense the cues with their whiskers or their body. The cueless belt was composed of a plain burlap material. For the GOL experiments, the 10 cm size reward zone was set to be at least 10 cm away from the closest tactile cue, so that animals did not associate the cue with the reward. All spatial information was presented to the mice via the treadmill belt. In addition, similar to head-fixed multisensory context configurations in our previous publications (Danielson et al., 2016; Lovett-Barron et al., 2014; Zaremba et al., 2017), a multisensory context was created using a continuous presentation of a constant odor (e.g., carvone), blinking red LED (e.g., 100-ms duration at 1 Hz) and an auditory tone (e.g., continuous beeps at 2 kHz, 100-ms duration at 1 Hz).

To assess the effect of the modulation of VIP+ IN activity on learning behavior (Figure 6A) and CA1 pyramidal cell activity (Figures 6B–6F), mice that were injected with VIP-ArchT, VIP-ChR2, and VIP-GFP (see above) were trained on the GOL behavior. The laser stimulation was set to a 70 cm segment of the belt centered around the reward zone. We used a continuous illumination strategy for activating ArchT, while for ChR we used 20Hz activation pattern with 50% duty cycle. We also included a 15 s long time out window to shut off the light delivery and protect the brain from photo-damage if the mouse spent more than 15 s in the reward zone. We applied continuous, matching color ambient LED illumination in the behavior rig to prevent mice from cuing on the light emitted by laser illumination.

Post hoc neurochemical identification of VIP+ INs

After the last imaging sessions mice were put under deep isoflurane anesthesia and trans-cardially perfused with 4% paraformaldehyde in 0.1 M PBS. After overnight post-fixation in the same solution the brains were transferred to PBS until sectioning. The upper 500 μm of the brains were sectioned horizontally into 50 μm thick sections with a vibratome. The sections were incubated in a mixture of anti-GFP (1/2000), anti-pro-CCK (1/250 – 1/500) and anti-Calretinin (1/200) antibodies (see Key Resources Table) for several days at 4°C, and then washed several times in PBS then transferred to the cocktail of secondary antibodies: a-chicken-AlexaFluor488 (1/500), a-rabbit-DyLight405 (1/100) or a-rabbit-AlexaFluor594 (1/200) and a-mouse-DyLight649 (1/200). After overnight incubation the sections were washed, and mounted on slides in the same orientation in the proper dorso-ventral order. The slices were scanned with a confocal microscope (Leica SP5) and then the Z stacks were visually inspected until a match with the recorded two-photon field-of-view was found. The neurochemical characteristics of the cells was determined based on the presence or absence of CCK or CR immuno-signal.

Immunocytochemical validation of VIP-IRES-Cre mouse line

Four hemizygous VIP-IRES-cre mice were injected with AAV2/1:Syn-(tdTomato)^{Cre} virus in CA1. Two weeks after the injections the mice were deeply anaesthetized with isoflurane then transcardially perfused with 40 mL 4% paraformaldehyde dissolved in 0.1 M phosphate buffered saline (PBS) solution. The brains were dissected out from the skull and kept in the perfusion solution overnight for postfixation. The immunocytochemical reactions were done on free-floating 50 μm thick, coronal vibratome slices. First the slices were subjected to an antigen retrieval procedure by incubating in 10 mM Sodium citrate solution supplemented with 0.05% Tween-20 (pH 6.0) at 95°C for 45 minutes. Then the sections were incubated in a cocktail of the following primary antibodies for two days: 1/8000 dilution of a-VIP raised in rabbit and 1/3000 dilution of a-RFP antibody raised in goat. The sections were then washed in PBS for several times. For detecting the VIP immunoreactivity, we applied a biotin-tyramide amplification step according to the instructions of the kit provided by the manufacturer (TSA Kit, Molecular Probes T20921). Finally, we incubated the sections in a cocktail containing avidine conjugated Cy5 (Molecular Probes, 1/400) and AlexaFluor594 conjugated anti-goat secondary antibody (1/300, Jackson ImmunoResearch). The sections were washed in PBS for several times, mounted on slides and coverslipped with Fluoromount-G mounting media. The sections were scanned with Leica SP5 confocal microscope equipped with the appropriate lasers (633 nm, 543 nm) and filter sets. We used 3-4 slices from dorsal hippocampus per mice to quantify number of the double labeled cells. Quantification of the double labeled cells were done on maximum Z projected confocal stacks (Figure 1A).

Monosynaptic retrograde rabies tracing

The method of *trans*-synaptic retrograde labeling is described elsewhere (Reardon et al., 2016). Briefly, VIP-IRES-Cre mice (n = 4) were injected in the left dorsal CA1 with a virus cocktail containing AAV2/1:EF1α-(TVA-mCherry)^{Cre} and AAV2/1-pAM-CAGGS:H2B-(3XHA-P2A-N2cG)^{Cre}. Two weeks after the priming injection, the mice were injected in the same spot with pseudotyped rabies virus (ENVA-CVS-N2c$^{\Delta G}$) expressing GFP. Mice were trans-cardially perfused with 4% PFA in 0.1 M PBS two weeks after the pseudotyped rabies injection. The brains were carefully removed from the skull, post-fixed in 4% PFA overnight and sliced up to 70 μm thick sections with a vibratome. GFP expression in all of the sections was enhanced with GFP immuno-staining and the HA tag in the starter cells was detected with rabbit a-HA antibody followed by incubation in donkey anti-rabbit-DyLight649. Sections

were mounted, coverslipped, and scanned for the GFP signal with a stereoscope (Nikon SMZ18) equipped with a custom motorized stage (Ludle) and with a high resolution digital camera (Flash Orca, v4.2, 2048x2048 resolution). We used a low magnification objective (Nikon 1x or 1.6x) to capture the images which were opened in ImageJ and the GFP positive cells were counted in each slice with the cell counter tool. The brain areas with GFP labeled cells were identified based on the Paxinos atlas (Paxinos and Franklin, 2004). Hippocampal slices with the starter cell labeling were scanned with a confocal microscope (Leica SP5) and the starter cells were counted and identified on individual confocal maximum projected Z stacks.

QUANTIFICATION AND STATISTICAL ANALYSIS

Ca^{2+} data preprocessing

The preprocessing steps of the raw fluorescence signal were described elsewhere (Danielson et al., 2016; Lovett-Barron et al., 2014). Briefly, the acquired frames were motion corrected with the SIMA software package (Kaifosh et al., 2014). In cases where motion artifacts were not adequately corrected, the affected data was discarded from further analysis. VIP+ INs and CA1 pyramidal cells (CA1PC) in FOVs were hand-segmented on time averaged images in ROIBuddy (Kaifosh et al., 2014) or ImageJ. For INs, the raw fluorescence signal was calculated from the ROIs using SIMA package across the imaging sessions. In experiments with optogenetic manipulations of VIP+ INs with simultaneous imaging of CA1 pyramidal cells (Figures 1C, 1D, S2A, S2B, and 6D–6F) VIP+ interneurons were directly identified based on their tdTomato expression, while other putative interneurons located in the pyramidal layer were identified based on the lack of clear GCaMP- Ca^{2+} transients in them, morphological criteria, and their higher baseline fluorescence (Zaremba et al., 2017), and were excluded from further analysis. In order to separate the CA1PC signals from potential neuropil contamination, the fluorescence signals of the CA1PC ROIs were processed using FISSA (Keemink et al., 2018) with the following parameters: 6 neuropil subregions, $\alpha = 0.2$, and 7 signal components.

We computed the relative fluorescence changes ($\Delta F/F$) with the baseline calculated using the method adopted from Jia et al. (Jia et al., 2011) (parameters: t1: smoothing window: 1 s for PC, 10 s for INs, t2: baseline size: 15 s for PCs, 100 s for INs). Furthermore, for PCs, we detected statistically significant transients as described previously (Danielson et al., 2016; Dombeck et al., 2010; Dombeck et al., 2007) to use in place field calculations. Further analyses of the GCaMP-Ca^{2+} and behavioral data were implemented in Python 2.7 and detailed below.

Signal analysis

Transient area under the curve (AUC) analysis

For each statically significant transients of PCs, the AUC of the transient is computed as the sum of the Ca^{2+} fluorescence signal during the transient duration, normalized by frame rate.

Measuring the disinhibitory effect of VIP+ IN activation

The experiments in Figures 1C, 1D, S2A, and S2B had a fixed belt spatial window where the LED is activated on alternating laps (see above). To measure the change in activity of a CA1PC to LED stimulation of VIP+ INs, we compared the mean $\Delta F/F$ and transient AUC in the LED spatial window for LED-on laps to the same spatial window in the LED-off laps, to control for potential spatial activity of CA1PCs. Furthermore, since CA1PC activity is sparse, we restricted our analysis to those CA1PCs that had at least one transient in the LED spatial window during both LED-on laps and LED-off laps.

Responses to behavioral events

For each Ca^{2+} trace triggered on an event, the mean of the pre-event activity was subtracted from the mean of the post event activity (mean $\Delta F/F_{post\text{-}event}$ – mean $\Delta F/F_{pre\text{-}event}$) to calculate the response magnitude. The time window for post-event and pre-event was 3 s. For locomotion responses (Figures 2C–2E), if a reward delivery event occurred within the pre or post locomotion event window (3 s pre and post), then that locomotion event was excluded. This was to avoid potentially mixing reward responses with locomotion responses. The exception to this was when we specifically examine the running-stop events that co-occurs with reward delivery (Figure 4), in which case we only included running-stop events where a reward delivery event occurred within the *pre* and *post* window (3 s).

Running modulation calculation

To determine the changes in Ca^{2+} activity due to animal locomotion and exclude potential transient responses from running-start and running-stop (Figure 2F), only the activity in rest and running intervals with durations greater or equal to 9 s was considered. The response of the Ca^{2+} activity of each cell for each interval was calculated as the mean of the 1 s Ca^{2+} activity centered on the middle of the interval.

Cross correlation between velocity and GCaMP Ca^{2+} activity of interneurons and locomotion group classification

The Ca^{2+} activity of INs of a recording session and the corresponding velocity of that session were first smoothed with a Gaussian kernel with a s.d. of 0.05 s. For each IN, the Ca^{2+} activity trace was then cross-correlated with the velocity with a limit that the minimum offset is −5 s (activity leading velocity) and the maximum is +10 s (activity lagging velocity). Since the same IN was cross registered across multiple sessions, the cross correlation curve for that IN was averaged across those sessions for all the days recorded (Figures 2B, 3B, and S3A). The peak and the lag were calculated from the optima of the averaged cross correlation curve for each cell.

Cells were classified as either positive velocity modulated (PVM) if the peak of the cross correlation curve is positive, or negatively velocity modulated (NVM) if the peak is negative, regardless of the lag time of the peak. For calculating the day-to-day stability of the

grouping identity of an IN (Figure S2D), the cross correlation curves of the sessions of each day were averaged, and the classification assigned based on the peak for that day. The classification of each IN was compared for one day to the next (consecutive pairs).

Controlling for the reward modulation of velocity

The reward modulation of velocity is calculated as mean(velocity$_{pre}$)$_{rewarded}$-mean(velocity$_{pre}$)$_{unrewarded}$ for pre-running-stop and mean(velocity$_{post}$)$_{rewarded}$-mean(velocity$_{post}$)$_{unrewarded}$ for post-running stop (Figure S3D). The velocity mean is using the mean of 3 s of velocity pre and post running-stop respectively. To remove the effect of the reward modulation of velocity and animal performance, the least-squares linear regression is calculated between the fraction of licks near the reward and the velocity modulation for both pre-running-stop and post-running-stop. The residual of the fraction of licks is calculated from the least-squares regression. To remove the effect of the reward modulation of velocity and VIP+ IN activity, the residual of the reward modulation of VIP+ INs' response against the velocity modulation is calculated similarly. The residuals are then correlated with each other.

General linear model (GLM)

We use a simple linear model to directly link the Ca^{2+} activity as a linear function of input vectors (i.e., behavioral variables). Fitting the GLM coefficients entails finding the linear combination of behavioral covariates which optimally predicts the Ca^{2+} signal of a VIP+ IN. The following behavior variables were used: velocity, running-start, running-stop, licking, position, and water (reward). All the variables (except position) were smoothed with a Gaussian kernel (σ = 0.125 s), and also shifted in time by ± 3 s (Figure 5A) to account for temporal correlations between predictors and the Ca^{2+} signal. This window was chosen based on our analysis of velocity cross-correlations, which showed a lag of 1-3 s for most VIP+ INs (Figure 2B). For the position signal, we divided the treadmill into 100 non-overlapping bins, which were represented in the model by 100 corresponding binary variables that were equal to one during times when the animal occupied that spatial bin and zero otherwise (Figure 5A). These behavior variables were fitted to the Ca^{2+} activity of a VIP+ IN using ridge regression (Pedregosa et al., 2011), to manage potential collinearity of predictors and avoid overfitting. For cross-validation, the Ca^{2+} activity was first divided into six 100 s blocks. Each block was further divided into 10 s intervals. We implemented a 10-fold cross-validation procedure, where we trained the model on nine of ten 10 s intervals (of all six 100 s blocks simultaneously), and then tested on the held-out intervals (Figure 5A). The intervals used for testing were then rotated in subsequent folds. We evaluated the model performance and comparisons on each cross-validation fold separately and combined these results to produce final summary statistics on model performance for each cell of each session. The regularization penalty was optimized separately through cross-validation on the training set, before fitting the final model on the full training set and evaluating prediction quality on the test set. To assess fit quality, we calculated the correlation coefficient and the coefficient of determination (r^2) between the model's predicted Ca^{2+} activity and the actual Ca^{2+} activity. The covariates that we considered in the model can be correlated, which could produce redundancies in the model. Therefore, to estimate the specific contribution of each category of behavior variables, we also trained a reduced model which contained all variable groups except the category of interest. We then calculated the (base-2) log-likelihood ratio between the full model and the reduced model, normalized by the number of time samples, to estimate the information gained (in bits/sample) for predicting VIP+ IN activity by including the missing variable group. Importantly this measure was also estimated only from the held-out test data in the cross-validation procedure (Harris et al., 2003).

Measuring the effect of the optogenetic laser on motivation to seek reward

To measure the effect of the optogenetics laser on the animal's motivation to seek reward (Figure 6A), we measured the change in the average velocity and rate of licking before and after the laser turned on. Therefore, we elected to examine how much the licking and velocity changes as we turn on the laser (Figure S5B). We performed this comparison only in the first session where the learning performance is comparable and only the laser activation events where there was no reward delivered, to avoid any learning performance related confounds. We took the average of the licking and velocity in a 5 s pre and 5 s post window of each event and subtracted the pre from the post to calculate the magnitude of the change for that event. The magnitude of change of the events are averaged by mouse.

Place cell analysis

Detailed methods for determining statistically significant place cells and their place fields, and the enrichment of the place fields around the reward zone are described in (Danielson et al., 2016; Zaremba et al., 2017). Briefly, for each pyramidal cell, Ca^{2+} transients whose onsets occurred during running bouts of at least 1 s in duration were used to calculate the spatial information (Skaggs et al., 1993) of that cell. Transients were then randomly reassigned to different times during the running epochs and the spatial information as recalculated. This random reassignment was done for 1000 iterations to create a null distribution for spatial information, and the cell was considered to be a place cell if its spatial information was above the 95 percentile of the null distribution. The place field of a place cell was calculated from its transient rate map over 100 spatial bins that evenly divide the belt. The rate map was the number of transients in a given spatial bin normalized by the animal's occupancy in that spatial bin, which was then smoothed with a Gaussian kernel (σ = 3 spatial bins). To detect individual place fields, each local maximum of the smoothed rate map was fitted with a Gaussian curve centered at that location. For each smoothed rate map, the place fields where the associated Gaussian was smaller than 50% of the largest Gaussian (by measuring the total area under the curve) were discarded. The remaining Gaussians were considered place fields, and the most active place field (the largest Gaussian by area under the curve) of each cell was used for the enrichment analysis in Figure 6F.

For analyzing spatial tuning of VIP+ INs in Figure S2G, the $\Delta F/F$ was used to calculate the spatial information of each cell. The $\Delta F/F$ is then circularly randomly shifted in time for 1000 iterations to create a null distribution for spatial information. A cell is considered to have significant spatial information if it is greater than 95% of the null distribution.

For the enrichment analysis (Figure 6F), we calculated the relative spatial location to the reward of the most active place field for each CA1PC place cell. If CA1PC place cells uniformly sampled the positions on the belt, then the expected fraction of place cells would be the same as the fraction of the belt measured, e.g., 15% of the cells in 15% of the lap near the reward position. If the place cell population preferentially represented positions near the reward, then the fraction of cells in the 15% of the belt near the reward position would be higher than 15%. For the analysis in Figure 6F, a one-sample t test was used to determine if the fraction of cells in each mouse in the 15% of the belt near the reward position was significantly higher than expected. The change between the fractions of cells near the reward position before and after learning was also calculated per mouse, and a one-sample t test was used to determine if the change was significantly different from zero.

Statistical analysis

For all standard statistical tests (detailed in figure legends), the α was chosen to be 0.05 for statistical significance. To correct for multiple comparisons, the α was divided by the number of tests according to the Bonferroni procedure. Throughout the figures, p values are denoted by * ($p < 0.05$), ** ($p < 0.01$), and *** ($p < 0.001$). Bootstrap statistical tests are detailed below.

Bootstrap for testing for significant running modulation of Ca^{2+} activity

For each cell, we pooled together the responses to the resting intervals and the running intervals (see *Running modulation calculation* above) into the resting pool and the running pool respectively. The two pools were sampled with replacement for 3000 iterations. For each iteration, the magnitude of the running modulation was calculated as the mean response of the sample from the resting pool subtracted from mean response of the sample from the running pool (mean $\Delta F/F_{running}$ - mean $\Delta F/F_{rest}$). The 3000 running modulation magnitudes are then used to construct a two-tailed 99% confidence interval (CI). A cell was considered to have a significant positive running modulation if CI is greater than 0, negative modulation if CI is less than 0, and no modulation if the CI contains 0.

Bootstrap for testing for significance of responses to behavior events

To calculate whether a cell reliably changed its activity for an event type (Figures 2C–2E, 3C, and 3D), the response magnitudes of the Ca^{2+} traces (see Responses to behavior events above) for that event type for that cell were pooled together, and then the pool was sampled with replacement for 3000 iterations. For each iteration, the mean response magnitude was calculated. The 3000 mean response magnitudes were then used to construct a two-tailed 99% confidence interval (CI). The cell was determined to have a significantly negative response if the CI was less than 0, a significantly positive response if the CI was greater than 0, and a non-significant response if the CI contained 0.

Reward modulation of running-stop responses

For the analysis in Figure 4, a two-sample bootstrap test was used to calculate whether a VIP+ IN's response to running-stop events was significantly modulated by reward presentation. For each VIP+ IN, the response of the cell to each of the running-stop event was calculated as in the Responses to behavior events section above. Each event as further classified as rewarded and unrewarded, by the criterion that reward was presented in the 3 s window pre and post the running stop event. The events of the two classifications were then pooled separately into rewarded and unrewarded pools. The two pools were sampled with replacement for 3000 iterations. For each iteration, the magnitude of the reward modulation was calculated as the mean response of the sample from the unrewarded pool subtracted from mean response of the sample from the rewarded pool (mean $response_{rewarded}$ - mean $response_{unrewarded}$). The 3000 reward modulation magnitudes are then used to construct a two-tailed 99% confidence interval (CI). A cell was considered to have a significantly positive reward modulation if CI is greater than 0, a significantly negative modulation if CI is less than 0, and not significant if CI contains 0.

Correlations with learning performance

For each metric measured, e.g., the predictive information gained from reward variables (Figure 5C), the mean of the metric of the cells were averaged for each session. For correlations of the PVM and NVM groups, only cells in the respective groups were included. The mean of the metric for the sessions were then correlated with the behavior performance (fraction of licks near the reward) for that session. The 99% bootstrap confidence interval of the regression was calculated by resampling the sessions with replacement, and the regression was calculated for each resampling iteration. This is repeated for 3000 iterations.

Bootstrap for testing significant difference in fractions

For the analysis in Figure S1D, to test whether the fraction of VIP+ INs in each group (e.g., positive velocity modulated, PVM) is significantly different between a category of VIP+ INs (identified by post hoc neurochemical identification, e.g., CCK+) and all of the recorded VIP+ INs, we produced a null distribution from the all of the VIP+ INs. For each iteration, we randomly drew (with replacement) a sample of cells from all of the VIP+ INs, with the size of the drawn sample being equal to the size of the category we are comparing. This was repeated for 10,000 iterations, and the two-tailed 99% confidence interval was constructed for the number of cells in each group (e.g., PVM) in the null distribution. The fraction of a group (e.g., PVM) of VIP+ INs in a category (e.g., CCK+) was considered significantly different from the same group (e.g., PVM) from all of the VIP+ INs if the number of cells in that category was outside of the 99% confidence interval of the null distribution.

Data analysis and figures were done using custom made software in Python 2.7.15™ (https://www.python.org/). Data were analyzed statistically using GraphPad Prism 8.0.0. To compare level of enrichment among different groups (learning stage x condition), fractions of place cells were analyzed using two-way analysis of variance (ANOVA) followed by paired t test (two-tailed) with Bonferroni's correction whenever statistical significance was observed. The same procedure was followed to compare mean firing rates among groups (position in the track x condition), but here unpaired t test was used for post hoc comparisons.

Computational modeling

see STAR Methods.

DATA AND SOFTWARE AVAILABILITY

The SIMA package for Ca^{2+} imaging analysis is freely available online (http://www.losonczylab.org/sima/1.3.2). Calcium imaging datasets can be obtained from Attila Losonczy upon request. The computational model is available for download from ModelDB https://senselab.med.yale.edu/modeldb/enterCode.cshtml?model=246546 (accession #: 246546) and the Poirazi lab web site: http://www.dendrites.gr.